**Supporting Information**

# Modulating Catalytic Properties of Targeted Metal Cationic Centers in Nonstoichiometric Mixed Metal Oxides for Electrochemical Oxygen Reduction

Samji Samira, John Carl A. Camayang, Krishna Patel, Xiang-Kui Gu* and Eranda Nikolla*

*Department of Chemical Engineering and Materials Science, Wayne State University, Detroit, MI, 48202*

* **Corresponding authors:** Xiang-Kui Gu (X-K. G.) and Eranda Nikolla (E. N.)

X-K. G.: *xkgu@wayne.edu*

E. N.: *erandan@wayne.edu*

## Methods

**Density functional theory (DFT) calculations:** Spin-polarized DFT calculations were performed using the Vienna ab initio Simulation Package (VASP).[1,2] The exchange-correlation interaction was described by Perdew-Burke-Ernzerhof (PBE) functional.[3] The Kohn-Sham equations were solved using a plane-wave basis set with a kinetic energy cutoff of 400 eV. Experimental analyses using electron microscopy and diffraction showed that rhombohedral perovskites were characterized by $(10\bar{2})$ and $(0\bar{1}\bar{2})$ surface facets. DFT calculations revealed that these two surfaces exhibited comparable adsorption energetics for ORR intermediates due to their similar atomic structures. Here, the B-site terminated $(10\bar{2})$ surface was used to represent the oxide surface and was modeled using a seven-layer slab model with a (1×2) unit cell.[4] However, similar trends would be expected using the $(0\bar{1}\bar{2})$ surface. The B-site terminated $(10\bar{2})$ surface of rhombohedral perovskite as observed in our experiments was modeled using a seven-layer slab model with a (1×2) unit cell.[4] A (3×3×1) *k*-point mesh was used to sample the surface Brillouin zone, and a 15 Å vacuum was introduced with correction of the dipole moment between the repeated slabs along the *z*-direction. During optimization, the bottom-two layers of the slab were fixed, while the remaining atoms and adsorbates were relaxed until the residual force was less than 0.02 eV/Å. We note that the DFT+U correction was not considered, since it has been reported that the DFT+U calculations are not effective at predicting the correct activity trends for oxygen electrocatalysis on perovskites.[4,5] To determine the effect of Hubbard U correction to the DFT exchange correlation functional on the energetics associated with ORR on 4*d*/5*d* transition metal cationic sites, the most promising Rh-based perovskites ($LaB_{0.94}Rh_{0.06}O_3$, B = Mn, Co, Ni, Cu) were studied as examples. A U correction value of 5.97 eV was used

for the Rh cations.[6] It was found that the volcano relationship between the calculated theoretical ORR overpotential and the Bader charge of Rh cations remained unaffected (Figure S25), with $LaNi_{0.94}Rh_{0.06}O_3$ still exhibiting the highest ORR activity. This suggests that the DFT+U correction would have limited effect on the ORR activity trend of the 4*d*/5*d* metal cationic active sites in different perovskite compositions.

The adsorption energies of O*, OH*, and OOH* intermediates were calculated using $H_2O$ and $H_2$ in gas phase as reference. For the Gibbs free energy calculations of the elementary steps, the energy of gas-phase $O_2$ was referenced with respect to gas-phase $H_2O$ and $H_2$ to avoid the current DFT drawbacks in describing $O_2$ in the gas phase.[7] The energy of the liquid phase $H_2O$ was derived from an entropic correction to the gas-phase $H_2O$ at 0.035 bar and 300 K.[8] In the catalytic cycle of proposed ORR mechanism in alkaline environments, the first step involved the one electron electroreduction of $O_2$ by reaction with a $H_2O$ molecule to form OOH*. The OOH* electrochemically dissociated to O* and $OH^-$ ion in the second step. The third step involved O* reaction with another $H_2O$ molecule to produce OH*, which finally desorbed as $OH^-$ ion in the last step. The Gibbs free energy change for each elementary step was calculated as:

$$\Delta G = \Delta E_{DFT} + \Delta ZPE - T\Delta S + eU \qquad \text{(eq. 1)}$$

where $E_{DFT}$ is the DFT calculated energy of each optimized system. Zero-point energies of the ORR intermediates were determined using the calculated corresponding vibrational frequencies, and the values of $\Delta S$ for $H_2O$, $O_2$, and $H_2$ were adopted from the literature.[8] Based on the Gibbs free energy diagrams for ORR on these 4*d*/5*d* metal cations (Figure S1), theoretical ORR overpotentials (defined as the difference between the equilibrium

potential and the highest applied potential at which all reaction steps were exothermic) were calculated.[8]

**Synthesis of $LaNi_{1-x}Rh_xO_3$ perovskites:** A previously reported citrate-based sol-gel approach was utilized to synthesize $LaNi_{1-x}Rh_xO_3$ ($0 \leq x \leq 0.02$; or $x = 1$).[9–11] Stoichiometric amounts of $La(NO_3)_3 \bullet 6H_2O$ (Sigma Aldrich, >99.999%), $Ni(NO_3)_2 \bullet 6H_2O$ (Sigma Aldrich, >97%) and $RhCl_3 \bullet xH_2O$ (Sigma Aldrich, > 99.9%) were used as precursors for synthesis. The metal precursors were dissolved in millipore water (>18.2 MΩ-cm). Citric acid (Anhydrous, Fisher Scientific, >99.9%) and ethylene glycol at a molar ratio of 1:1.1:1.1 (total metal ions: citric acid: ethylene glycol) were used as the chelating and complexing agents, respectively. For the synthesis of $LaRhO_3$, ethylene glycol (Sigma Aldrich, >99%) and citric acid with a molar ratio of 2:3 were used in the gelation process.[10] The resultant solution was heated at 90°C to facilitate water evaporation and the formation of a gel. The formed gel was combusted at 400°C for three hours to facilitate the decomposition of the inorganic compounds, as well as the complete water removal, resulting in the formation of metal oxide precursor particles. The precursor was then crushed and subsequently calcined to facilitate crystallization into the appropriate oxide structure. A calcination temperature of 850°C was used to achieve phase pure $LaNi_{1-x}Rh_xO_3$ ($0 \leq x \leq 0.02$), while pure $LaRhO_3$, was obtained at 1000°C.

**Synthesis of the supported catalysts:** Incipient wetness impregnation was used to synthesize Rh supported on $LaNiO_3$ control catalysts. Solutions of the Rh salt precursor ($RhCl_3 \bullet xH_2O$) were sequentially impregnated onto $LaNiO_3$, followed by calcination at 700-850°C. Calcination of $RhCl_3 \bullet xH_2O$ in air at temperatures beyond 700°C leads to formation

of primarily $Rh_2O_3$ particles), as confirmed via XPS, and consistent with previous reports.[12] These oxides are referred to as *w* wt% $Rh_2O_3/LaNiO_3$ where $0.15 \leq w \leq 0.58$.

**Characterization:** Powder X-ray diffraction (XRD) patterns were acquired using a Bruker Phaser2 diffractometer equipped with a Cu K-α source (λ = 1.54 Å) in a 2θ range of 20 to 80° with a step size of 0.01°. Rietveld refinement of the XRD pattern was performed using General Structure Analysis System (GSAS) with a graphical user interface (EXPGUI). Crystal structure of $LaNi_{0.99}Rh_{0.01}O_3$ was refined using the rhombohedral ($R\bar{3}c$) space group. The occupancies of Ni and Rh were adjusted to 0.99 and 0.01, respectively, to represent the true composition of the oxide. The background was modeled using a shifted Chebyshev polynomial function, while the scale factor, background, peak shape, lattice constants and isotropic displacement parameters were refined. Residual $R_{wp}$ values and the goodness of the fit via visual inspection were used to determine the phase purity of the samples. High resolution transmission electron microscopy (HR-TEM), high angle annular dark field imaging using scanning transmission electron microscopy (HAADF-STEM) and energy dispersive X-ray spectroscopy (EDS) mapping were performed using a Talos F200X microscope (Thermo Fisher Scientific, USA) equipped with a field emission electron source. An acceleration voltage of 200 keV was used for all studies. Super-X EDS with four windowless silicon drift (SDD) detectors was used for high sensitivity to all elements during EDS elemental analysis. A Gatan double tilt sample holder was used to align the particle along the zone axis. TEM grids were prepared via dispersion of the oxide in methanol, followed by drop casting on a 300 Mesh ultrathin Au grid (Ted Pella), and subsequently heated at 120°C overnight. The Brunauer-Emmet-Teller (BET) surface areas of these oxides were measured via $N_2$ physisorption studies at 77K, using

Micromeritics ASAP 2020. Prior to analysis, the samples were degassed at 350°C for 90 minutes. Agilent 7700x inductively coupled plasma mass spectrometer (ICP-MS) was used to confirm the weight fraction (wt%) of Rh in various oxide systems. 15 mg oxide sample was initially digested in a 2:1 volume mixture of concentrated $HNO_3$ (Sigma Aldrich, ACS grade) and $H_2O_2$ (30 wt%, Sigma Aldrich). To ensure complete digestion, the sample was placed in an autoclave along with the desired solvents at 210°C for four hours. Upon cooling, the sample was diluted in 2 wt% $HNO_3$ before ICP-MS analysis. To analyze the metal leaching from the oxide in the electrolyte solution during electrochemical testing, the solution was digested in a 2:1 volume mixture of concentrated $HNO_3$ and $H_2O_2$. The mixture was allowed to rest overnight, before further dilution in 2 wt% $HNO_3$ for ICP-MS analysis. The detection limit of the instrument used for ICP-MS analysis (Agilent 7700x ICP-MS) was determined via the standard solutions employed for the calibration (Table S10).

High resolution X-ray photoelectron spectroscopy (HR-XPS) studies of the La 4*d*, Ni 3*p*, and Rh 3*d* regions were performed using Thermo Fisher NEXSA XPS equipped with a monochromatic Al-Kα source with an energy of 1486.6 eV. Due to significant overlap between the La 3*d* and Ni 2*p* spectra, La 4*d* and Ni 3*p* core-level regions were used for analysis. NEXSA consists of a 125 mm mean radius, full 180° hemispherical analyzer with a 128-channel position sensitive detector. $Ar^+$ sputtering was used for charge neutralization, because of the less conductive nature of the oxides. XPS measurements were conducted with a step size of 0.1 eV. Pass energies of 160 eV and 25 eV were used for the survey scans and the high-resolution analysis, respectively. A Shirley type background was used for all analysis, followed by subsequent background subtraction.

XPS peak fitting was performed using a Gaussian-Lorentzian function defined in CasaXPS for all elements. Special care was taken to pelletize powder samples with a force of 4860 psi (13 mm diameter) to ensure flat surfaces for angle resolved-XPS (AR-XPS) studies. Such an approach has been successfully used previously to obtain sensitive near surface information using XPS, AR-XPS, and low energy ion scattering spectroscopy studies (LEIS) using pelletized-powder samples.[13–17] Pelletized oxide samples were tilted between 0° (as reference) to 70° with a step of 35°. This resulted in a detection depth (*d*) between 4.75 nm at 0° to 1.6 nm at 70°.

Iodometric titrations involve the initial reduction of the transition metal (B) cations to a +2 oxidation state via reaction with $I^-$ ions (e.g., $2B^{3+}+2I^-\rightarrow 2B^{2+}+I_2$). The $I_2$ generated in the process is further reduced by the excess $I^-$ ions to form $I_3^-$ ( $I_2+I^-\rightarrow I_3^-$ ). The amount of $I_3^-$ formed is determined using titration with a standard solution of sodium thiosulfate ($I_3^-+2S_2O_3^{2-}\rightarrow 3I^-+S_4O_6^{2-}$). These experiments were performed by digesting 15-20 mg oxide samples in 2M HCl in a three necked round bottom flask. This was followed by injection of 2M KI solution in an Ar saturated environment using a Schlenk line setup, forming a dark yellow/brownish color solution. The three-necked flask was sealed with a septum to ensure minimal exposure to atmospheric air. Titration was initiated by the addition of 0.02M sodium thiosulfate solution using a burette, until the color of the solution turned pale. At this point, 1-2 mL saturated starch solution was injected as an indicator of the titration, forming a dark blue/black color solution. The titration continued until the solution became colorless.

**Electrochemical Measurements:** High surface area acid treated Vulcan XC-72R graphitic carbon (Fuel Cell Store) was used as the conductive support for the synthesized oxides.

The as received commercial Vulcan XC-72R carbon was treated with concentrated $HNO_3$ (Sigma Aldrich, ACS grade) at 80°C for 12 hours to remove all traces of metal impurities present in the carbon during its seeded growth synthesis.[18] The acid treatment of the carbon was subsequently followed by washing with copious amount of millipore water (~6-7 L) to neutralize the acidity. Commercial 20 wt% Pt/C and 5 wt% Rh/C (Sigma Aldrich) were used to benchmark the electrochemical studies.

Thin-films of the catalysts used for the electrochemical measurements were prepared by drop-casting slurries on a glassy carbon support (Pine Research, 5 mm diameter). These slurries were prepared by ultrasonicating a mixture containing a 5:1 mass ratio of the synthesized oxide and carbon, in a solution of 2:1 volume ratio of millipore water (>18.2 MΩ-cm) and 2-propanol (Sigma Aldrich, > 99.9%). A 5 wt% Nafion solution (Ion Power) was used as the binder in these studies. The glassy carbon support was polished to a mirror finish using 50 nm alumina slurry, followed by further sonication in millipore water and 2-propanol. The glassy carbon support was then placed in a Teflon tip, which was also further cleaned via sonication in millipore water and 2-propanol. The tip assembly was then dried by rotational air drying at 1600 rpm for 20 min. Finally, 10 µL of the slurry was drop-casted on the inverted shaft assembly containing the glassy carbon support, followed by rotational drying of the ink at 700 rpm. The resultant amounts of the oxide catalyst, carbon and Nafion were consistently set for all catalytic systems at 250, 50 and 50µg $cm^{-2}_{geo}$, respectively.

A standard three-electrode system consisting of a rotating disk electrode (RDE) as the working electrode was used for all electrochemical measurements. 0.1M KOH (Sigma Aldrich, Semiconductor grade, >99.99%) was used as the electrolyte solution for these

studies. Pt-wire and graphite rod (Pine Instruments) were used as counter electrodes to validate that no artifacts in the measured electrochemical performance arose from the nature of this electrode. Hg/HgO in 20 wt% saturated KOH solution (Koslow Scientific Company) electrode was used as the reference electrode. All the potentials in the electrochemical measurements were referenced to the Hg/HgO electrode and reported with respect to reversible hydrogen electrode (RHE). A custom-built 40 mL electrochemical cell was used for all activity measurements. The reported electrochemical studies were corrected for the internal resistance ($E - E_{iR}$), which was determined using high frequency impedance studies. A constant internal resistance of ~53.5 Ω was found for all these studies and was subsequently corrected. Linear sweep voltammetry (LSV) was performed at a scan rate of 10 $mVs^{-1}$ in Ar-saturated electrolyte (used as background current), or $O_2$-saturated electrolyte. The polarization curves were background subtracted to showcase the intrinsic electrocatalytic activity of the oxides.

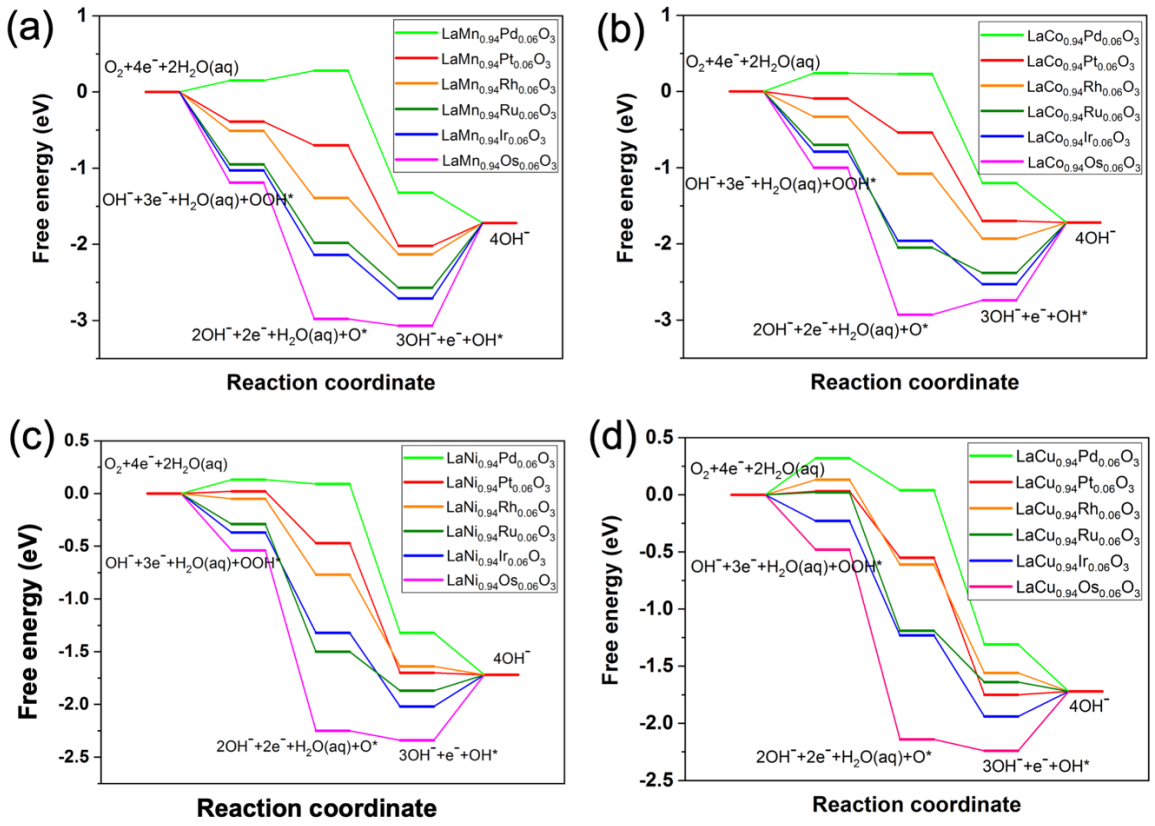


**Figure S1.** Free energy diagrams for ORR on $LaB_{0.94}B'_{0.06}O_3$ (B = Mn, Co, Ni, and Cu; B' = Pd, Pt, Rh, Ru, Ir, Os) at a typical fuel cell operating potential of 0.80 V vs. RHE (reversible hydrogen electrode).

Based on these free energy diagrams, a volcano relationship between the calculated theoretical ORR potential and the adsorption energy of OH* was observed as shown in Figure 1b in the main manuscript, where the pure $LaMnO_3$, $LaCoO_3$, and $LaNiO_3$ were also included as benchmarks.[4] The ORR activity comparison of these pure perovskites and their 4*d*/5*d* metal cations modified structures is important to understand the nature of the active sites and the effectiveness of embedding the 4*d*/5*d* metal cations in the perovskite structures to improve the oxide ORR activity. It was found that $LaMn_{0.94}B'_{0.06}O_3$ (B' = Os, Ir, Ru)

exhibited lower activity than $LaMnO_3$ due to their much stronger adsorption of OH* than $LaMnO_3$, suggesting that these metal cations would be poisoned by OH* during ORR, and thus Mn most likely would remain the active center similar to $LaMnO_3$. Contrarily, $LaMn_{0.94}B'_{0.06}O_3$(B' = Pt, Pd,) exhibited improved ORR activity when compared to $LaMnO_3$, suggesting that Pt and Pd cations would be the ORR catalytic active centers in these oxides. Similarly, B' cations in $LaCo_{0.94}B'_{0.06}O_3$ (B' = Os, Ir, Ru) would also be poisoned by OH*, while Pt and Pd cations would lead to enhanced activity as compared to $LaCoO_3$. In the case of $LaNi_{0.94}B'_{0.06}O_3$, it was found that all these metal cations except for Os exhibited higher ORR activity than $LaNiO_3$, suggesting that these metal cations would be the active sites.

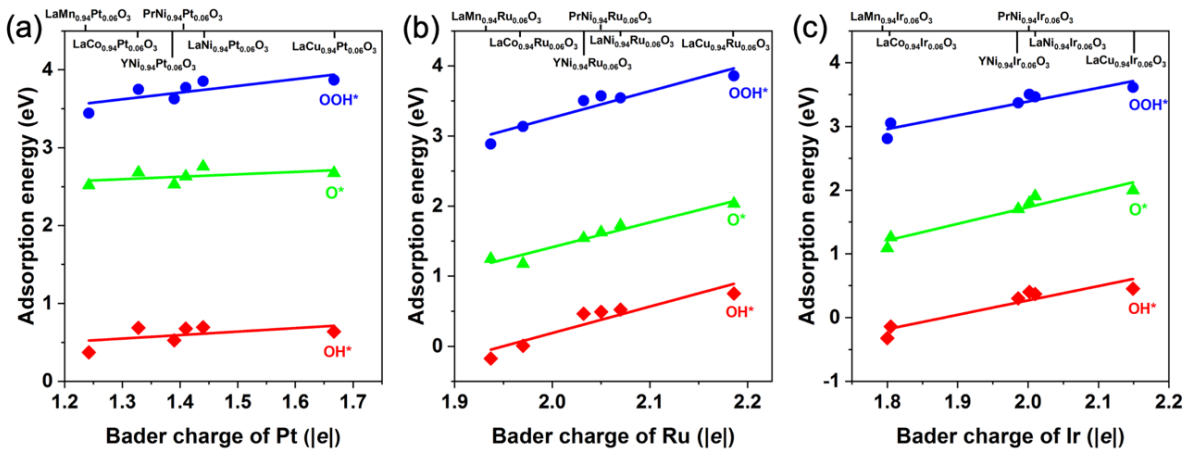


**Figure S2.** Adsorption energies of ORR intermediates on $AB_{0.94}B'_{0.06}O_3$ (A = Y, La, and Pr; B = Mn, Co, Ni, and Cu; B' = Pt **(a)**, Ru **(b)**, and Ir **(c)**) as a function of the Bader charges of surface B' metal cations.

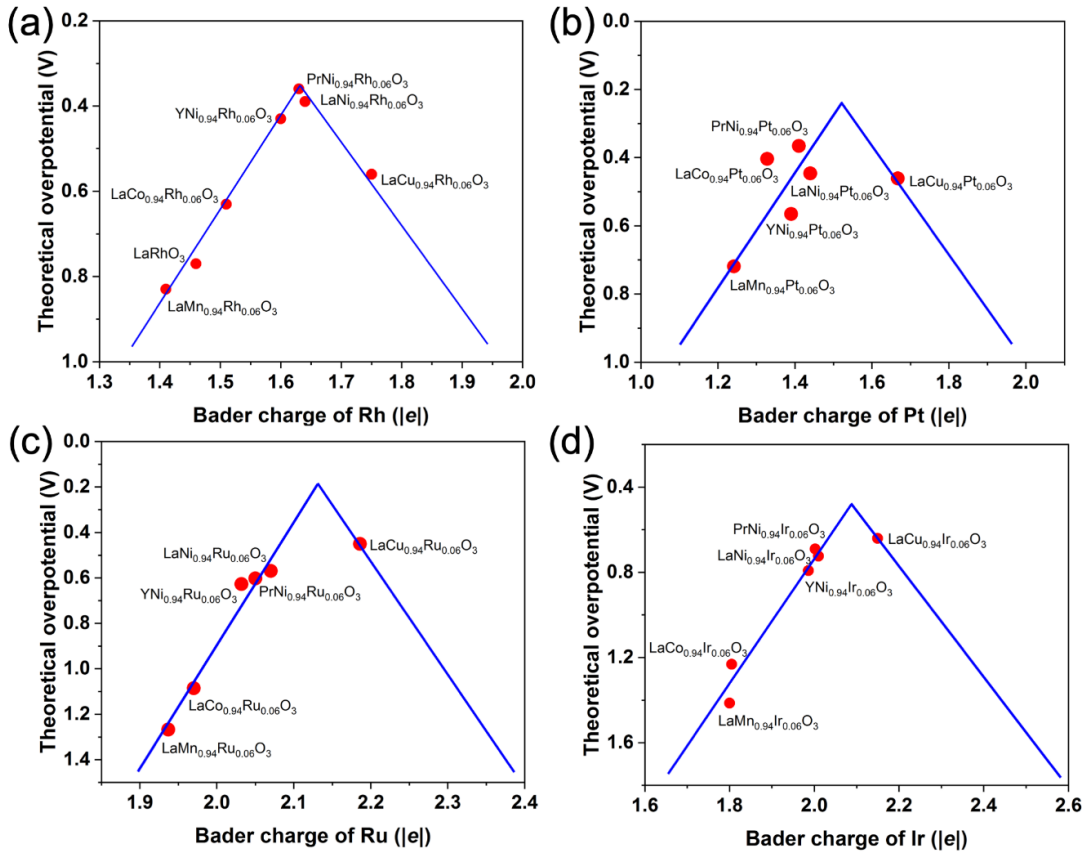


**Figure S3.** Volcano relationships between the theoretical ORR overpotentials on $AB_{0.94}B'_{0.06}O_3$ (A = Y, La, and Pr; B = Mn, Co, Ni, and Cu; B' = Rh **(a)**, Pt **(b)**, Ru **(c)**, and Ir **(d)**) as a function of the Bader charges of surface B' metal cations. An optimal electronic structure of the B' metal cations is required to achieve the lowest ORR overpotentials. The deviation in the volcano relationship in (**b**) between the Bader charge of Pt cations in $AB_{0.94}Pt_{0.06}O_3$ oxides and the theoretical ORR overpotential is a result of the adsorbate induced structural changes in the terms of Pt–O (lattice O and hereafter) bond distance in the oxide structure. For instance, the Pt–O bond distance in $LaNi_{0.94}Pt_{0.06}O_3$ was elongated by 0.03 Å upon OH* adsorption on the Pt cation when compared to the clean oxide surface. The longer Pt–O bond distance results in a less oxidized Pt, lowering the Bader charge of the Pt cation when compared to the same Pt cation in a clean surface. This, consequently,

induces deviation in the dependence of the theoretical ORR overpotential on the Bader charge of Pt cations obtained from a clean oxide surface.

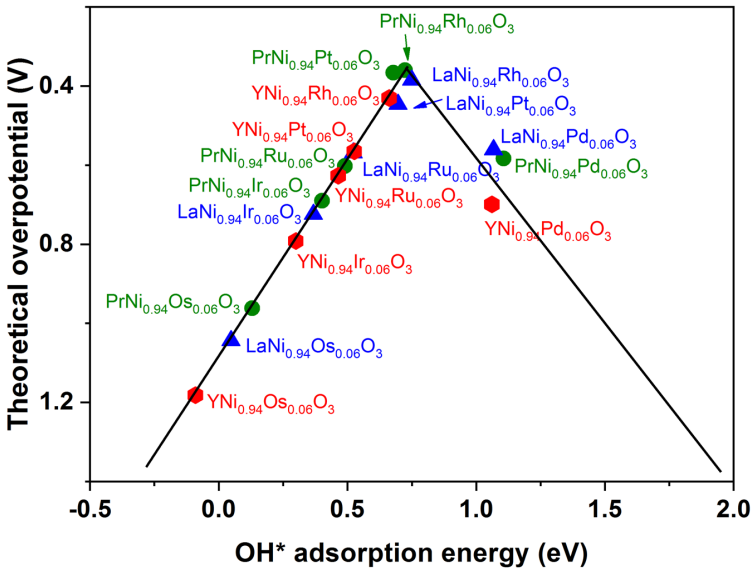


**Figure S4.** Volcano relationship between the calculated theoretical ORR overpotential and the adsorption energy of OH* for ORR on $ANi_{0.94}B'_{0.06}O_3$ (A = Y, Pr, La; B' = Pd, Pt, Rh, Ru, Ir, Os).

To determine the effect of the perovskite A-site composition on the activity of highly dispersed B'-site 4*d*/5*d* metal cations for ORR, $ANi_{0.94}B'_{0.06}O_3$ (A= Y, Pr, La; B' = Pd, Pt, Rh, Ru, Ir, Os) perovskites were considered. The calculated adsorption energies of O*, OH*, and OOH* intermediates are shown in Table S2. It was also found that the adsorption energies generally became stronger as the metal cation varied from Os, Ir, Ru, Rh, Pt to Pd. Among the various A-site compositions, $YNi_{0.94}B'_{0.06}O_3$ perovskites generally exhibited stronger adsorption as compared to $LaNi_{0.94}B'_{0.06}O_3$ and $PrNi_{0.94}B'_{0.06}O_3$ for intermediates adsorbed on a specific B' metal cation. From the calculated Gibbs free energy changes of the elementary steps, it was found that OOH* formation was the potential determining step on $YNi_{0.94}Pd_{0.06}O_3$, while the ORR activity

was limited by OH* removal on the other $YNi_{0.94}B'_{0.06}O_3$ perovskites. The activity of $PrNi_{0.94}B'_{0.06}O_3$ (B' = Pd, Pt, Rh) was limited by OOH* formation, while OH* removal was the potential determining step on $PrNi_{0.94}B'_{0.06}O_3$ (B' = Os, Ir, Ru). From the calculated theoretical ORR overpotentials, it was found that specific 4*d*/5*d* metal cations embedded in $PrNiO_3$ generally showed the highest activity, followed by those in $LaNiO_3$, and $YNiO_3$.

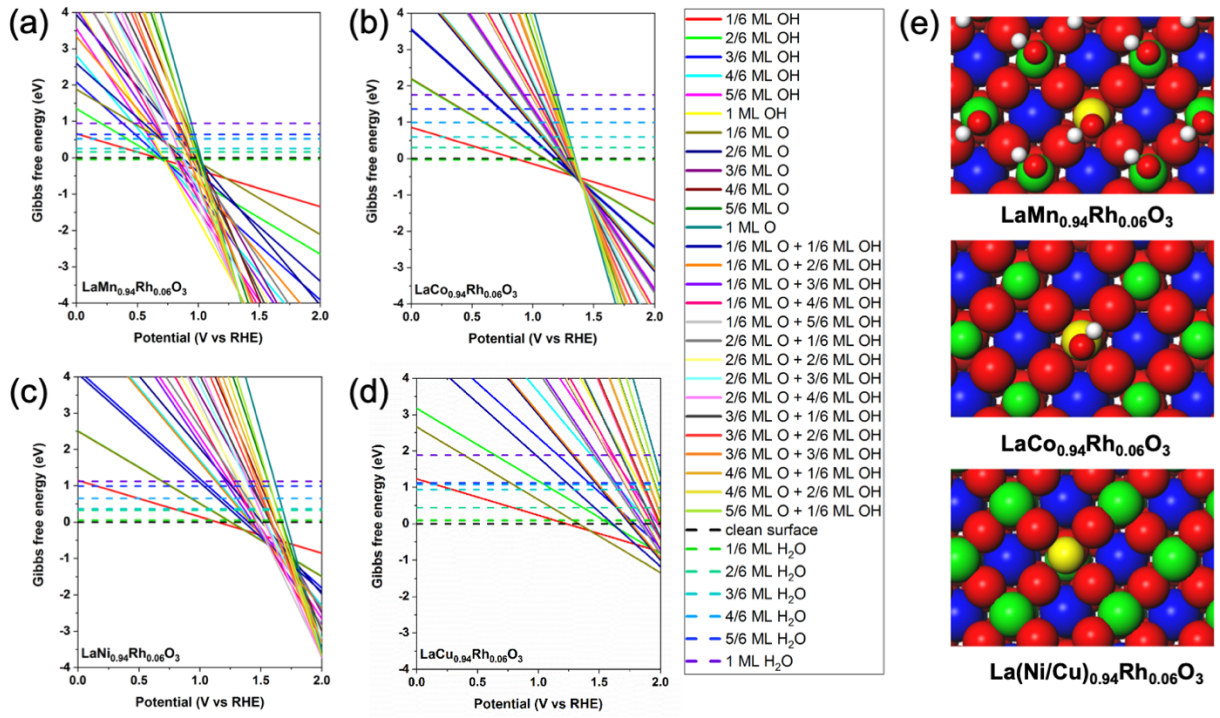


**Figure S5.** Surface phase diagrams for $LaB_{0.94}Rh_{0.06}O_3$ (B = Mn **(a)**, Co **(b)**, Ni **(c)**, and Cu **(d)**) as a function of potential at a constant pH of 13, and **(e)** the identified most thermodynamically stable surface structures for these oxides under typical ORR conditions. The blue, green, yellow, red, and white spheres represent La, B, Rh, O, and H atoms, respectively.

To determine the active surface phases of $LaB_{0.94}B'_{0.06}O_3$ under ORR conditions, surface phase diagrams were constructed using a previously reported approach[19], where it was assumed that the surface of the electrocatalyst interacted with an interfacial water layer at a given pH and potential. This resulted in adsorbed $H_2O$* along with OH* and O* on the surface from water dissociation with release of protons and electrons, as described by reaction steps 1-3.

$H_2O(aq) + * \rightarrow H_2O*$ (reaction 1)

$H_2O(aq) + * \rightarrow OH* + H^+ + e^-$ (reaction 2)

$H_2O(aq) + * \rightarrow O* + 2H^+ + 2e^-$ (reaction 3)

The Gibbs free energy changes for water adsorption as well as OH* and O* formation were calculated using equations 2-4, respectively.

$$\Delta G_1 = E_{H_2O*} - E_* - E_{H_2O(aq)} + \Delta ZPE - T\Delta S \quad \text{(eq. 2)}$$

$$\Delta G_2 = E_{OH*} + 1/2\, E_{H_2} - E_* - E_{H_2O(aq)} + \Delta ZPE - T\Delta S - eU \quad \text{(eq. 3)}$$

$$\Delta G_3 = E_{O*} + E_{H_2} - E_* - E_{H_2O(aq)} + \Delta ZPE - T\Delta S - 2eU \quad \text{(eq. 4)}$$

As examples, Figure S5 shows the constructed surface phase diagrams for $LaB_{0.94}Rh_{0.06}O_3$ (B = Mn, Co, Ni, and Cu) at a constant pH of 13, consistent with the experimental conditions.

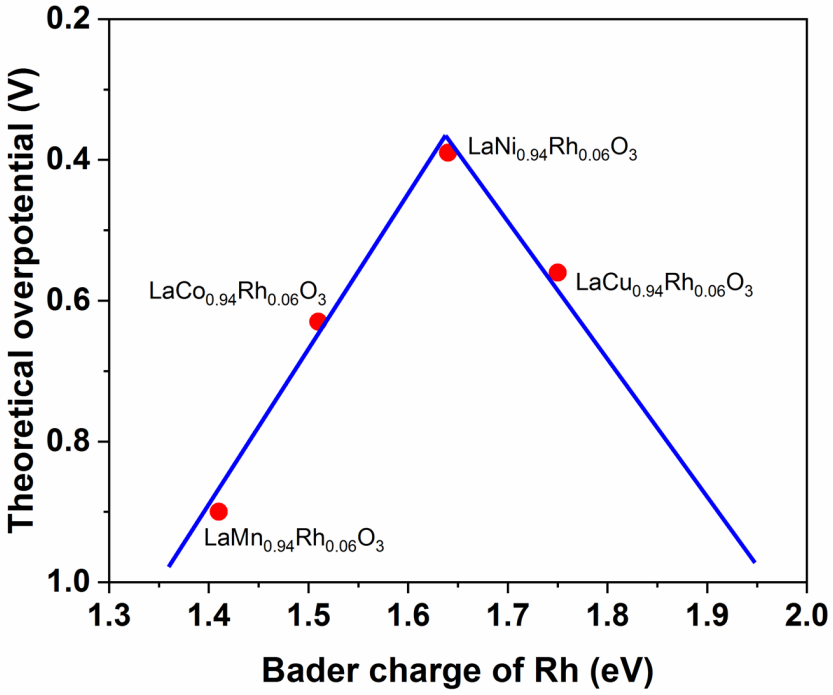


**Figure S6.** Volcano relationship between the calculated theoretical overpotential for ORR on the active surfaces of $LaB_{0.94}Rh_{0.06}O_3$ (B = Mn, Co, Ni, and Cu) and the Bader charge of surface Rh cations in these oxides. The following active surfaces were used in the calculations: clean surfaces of $LaNi_{0.94}Rh_{0.06}O_3$ and $LaCu_{0.94}Rh_{0.06}O_3$, the surface Rh cation of $LaCo_{0.94}Rh_{0.06}O_3$ covered by OH* (1/6 ML), and 1 ML OH* covered surface of $LaMn_{0.94}Rh_{0.06}O_3$. We note that the active sites in these oxide surfaces remain the Rh cations, with OH coverage mainly affecting the order of the steps in the ORR reaction mechanism. On clean Rh cations, the first step in the catalytic cycle is OOH* formation, while on OH* covered Rh cations, the first step is OH* desorption as $OH^-$.

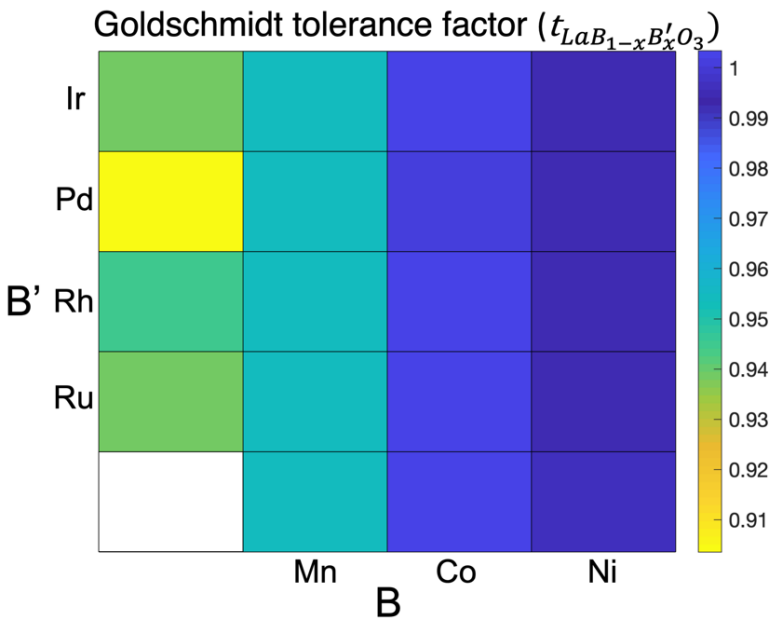


**Figure S7.** Phase stability evaluation via the calculated Goldschmidt tolerance factor (*t*) for various $LaB_{1-x}B'_xO_3$ (*x*=0, 0.01 and 1) oxides. Higher phase stability is characterized by a value of *t* ranging from 0.825 to1.059. More details regarding the tolerance factor (*t*) calculations can be found in Table S3.

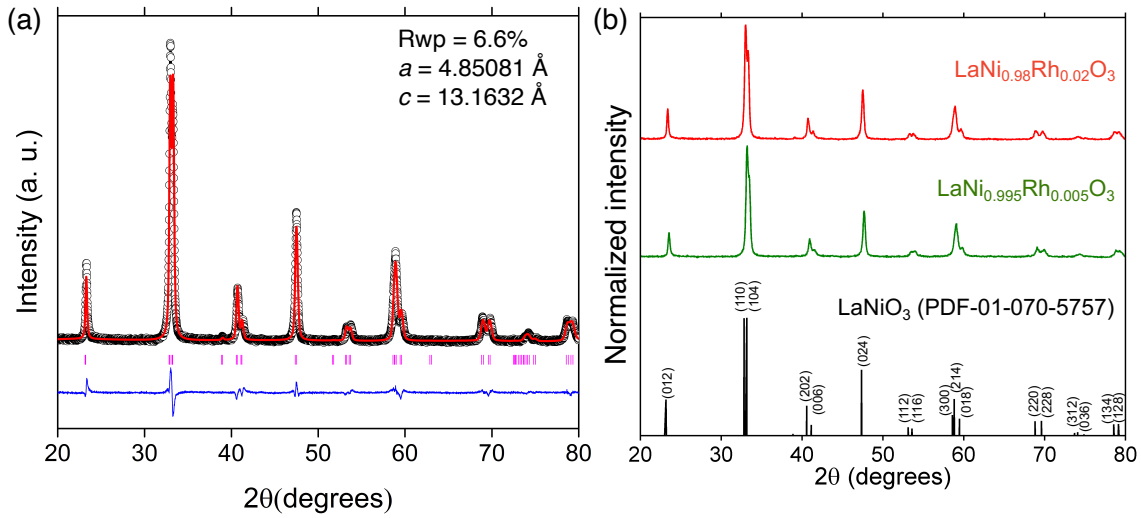


**Figure S8.** **(a)** Rietveld refined X-ray diffraction pattern of $LaNi_{0.99}Rh_{0.01}O_3$ confirming the formation of rhombohedral structure belonging to $R\bar{3}c$ space group. **(b)** XRD patterns of $LaNi_{0.995}Rh_{0.005}O_3$ and $LaNi_{0.98}Rh_{0.02}O_3$ in comparison with rhombohedral $LaNiO_3$ suggesting phase pure structures.

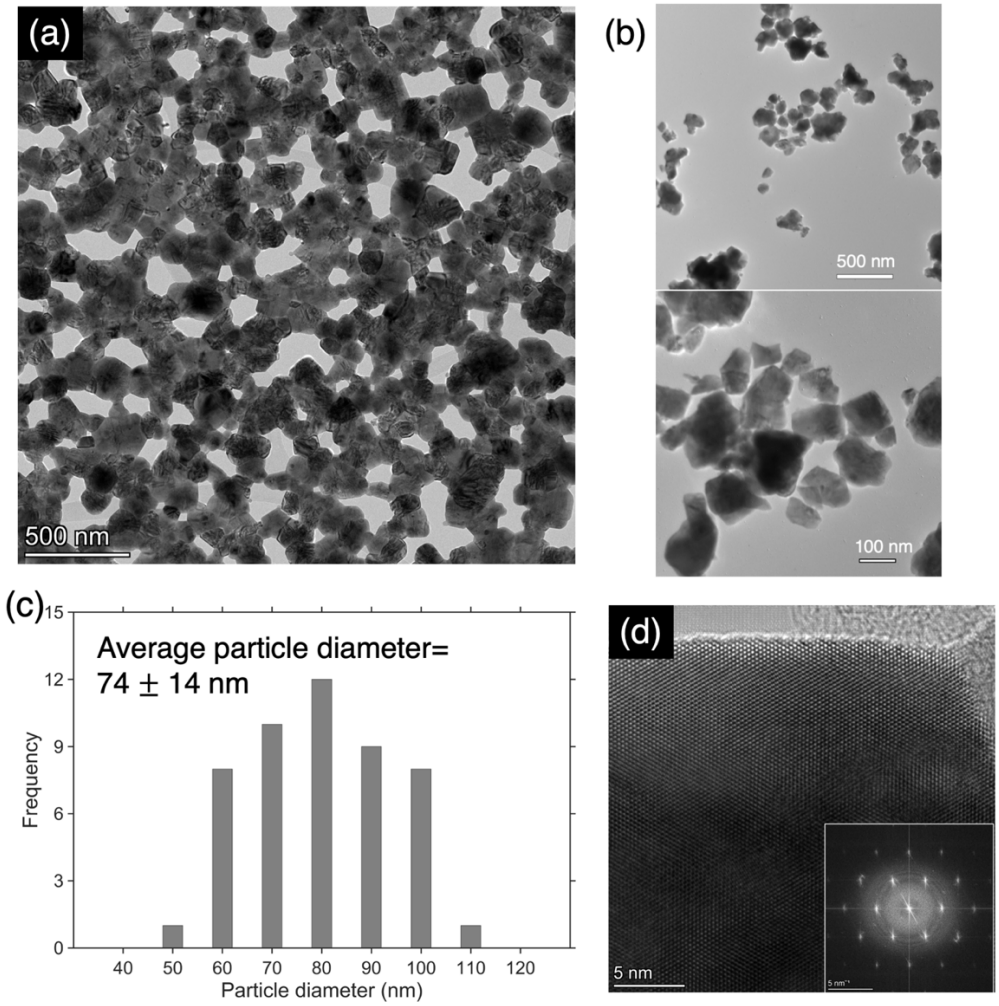


**Figure S9. (a-b)** Transmission electron micrographs (TEM) of $LaNi_{0.99}Rh_{0.01}O_3$. General representation of the particles is shown in **(a)**. Example micrographs of dispersed oxide particles used to estimate particle size distribution of $LaNi_{0.99}Rh_{0.01}O_3$ are shown in **(b)**. **(c)** Corresponding histogram of particle size distribution from TEM imaging for $LaNi_{0.99}Rh_{0.01}O_3$. These measurements were performed across multiple micrographs of particles similar to (**b**) and over 50 particles were used to estimate the particle size distribution. **(d)** High resolution (HR) TEM micrograph of the near surface region of $LaNi_{0.99}Rh_{0.01}O_3$ indicating the presence of continuous lattice fringes, consistent with crystalline nature of the oxide.

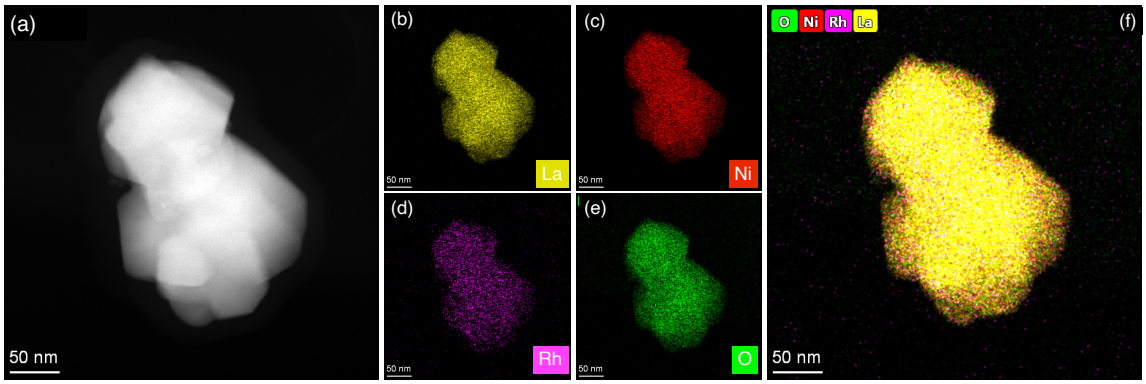


**Figure S10.** **(a)** High angle annular dark field imaging using scanning transmission electron microscopy (HAADF-STEM) of an individual particle of $LaNi_{0.98}Rh_{0.02}O_3$. **(b-f)** Energy dispersive X-ray spectroscopy (EDS) mapping of the particle in (a), indicating uniform distribution of La, Ni, Rh and O.

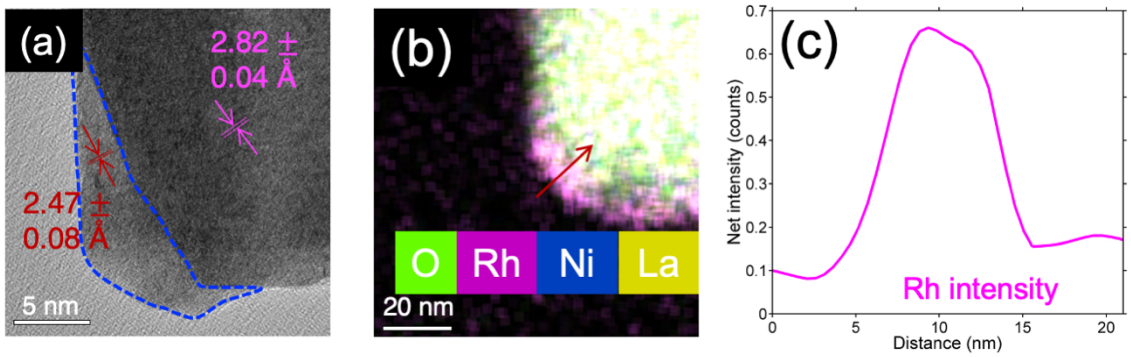


**Figure S11. (a)** HR-TEM micrograph of a supported $Rh_2O_3/LaNiO_3$ catalyst. Presence of $Rh_2O_3$ on the support $LaNiO_3$ is highlighted in blue in combination with the corresponding *d* spacing measurements. The *d* spacing of $Rh_2O_3$ (2.47 ± 0.08 Å) is consistent with the (211) lattice plane of $Rh_2O_3$.[20] **(b)** EDS mapping of La, Ni, Rh and O showing Rh supported on the surface of $LaNiO_3$. **(c)** EDS line-scan analysis for the region along the arrow showing the Rh signal mainly concentrated on top of the $LaNiO_3$ particle.

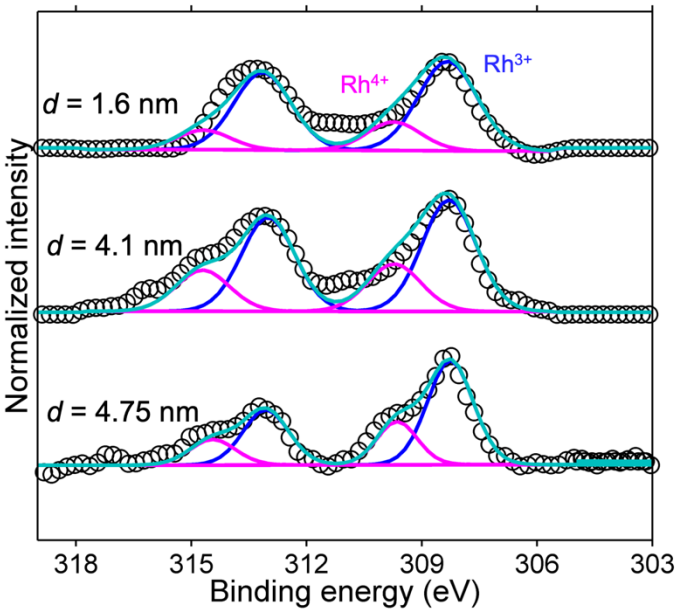


**Figure S12.** Angle resolved X-ray photoelectron spectra (AR-XPS) of Rh 3*d* for $LaNi_{0.99}Rh_{0.01}O_3$ at varying detecting depths (*d*) of 1.6-4.75nm. Mixed +3/+4 oxidation states of Rh were observed for all the detecting depths, indicating the highly oxidized nature of the Rh cations in the oxide. The experimental raw data is represented in black spheres. The blue and magenta curves represent the $Rh^{3+}$ and $Rh^{4+}$ fit of the Rh 3*d* 5/2 and 3*d* 3/2 curves, respectively. The teal-colored curve represents the overall fit. Slight decrease in the oxidation state of Rh was observed with decreasing detection depth (*d*). This was attributed to the increased sensitivity toward the under coordinated metal cations at the top surface layer of the oxide as detection depth decreased. The areas under the curve-fit of the raw data were used to quantify the Rh and Ni concentrations as a function of the detection depth, which are tabulated in Table S7.

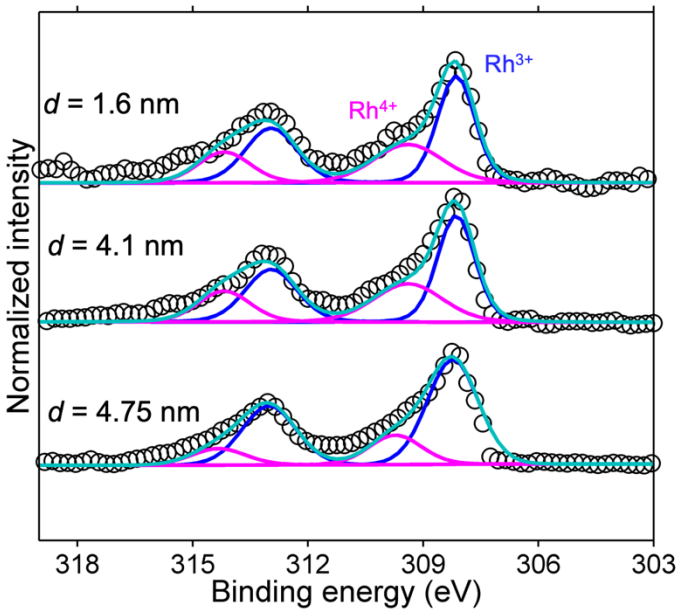


**Figure S13.** AR-XPS spectra of the Rh 3*d* region for 0.29 wt% $Rh_2O_3/LaNiO_3$ (control catalyst) at varying detecting depths (*d*) of 1.6-4.75 nm. Rh exhibited an average oxidation state of +3.16 indicating the formation of $Rh_2O_3$. The experimental raw data are represented with black spheres. The blue and magenta curves represent the $Rh^{3+}$ and $Rh^{4+}$ fit of the Rh 3*d* 5/2 and 3*d* 3/2 curves, respectively. The teal-colored curve represents the overall fit. The areas under the curve-fit of the raw data are used to quantify the Rh and Ni concentrations with varying detection depths in these systems, which are tabulated in Table S7.

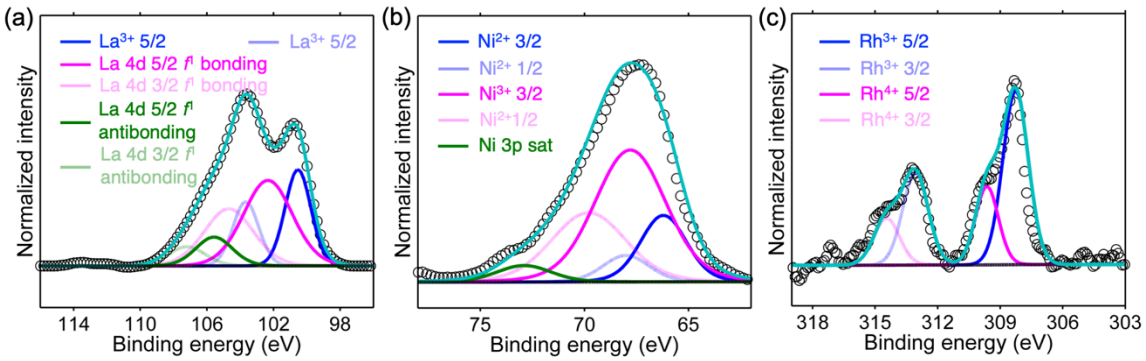


**Figure S14.** HR-XPS spectra of all the metals in $LaNi_{0.99}Rh_{0.01}O_3$. **(a)** HR-XPS spectra of the La 4*d* region indicating La to be present primarily in a +3 oxidation state. The blue fit indicates the $La^{3+}$ fit ($3d^9\ 4f^0$), while the magenta and green fits indicate the $4f^1$ bonding and antibonding contributions from $La^{3+}$ cations due to electron transfer to the nearby O ligand, for the 5/2 and 3/2 regions, respectively. **(b)** HR-XPS spectra of the Ni 3*p* region indicating a mixed +2/+3 oxidation state of Ni. The blue, magenta, and green fits represent $Ni^{2+}$, $Ni^{3+}$, and satellite, respectively. **(c)** HR-XPS spectra of the Rh 3*d* region indicating a mixed +3/+4 oxidation state of Rh, with an average oxidation state of +3.28 ± 0.01. The blue and magenta fits indicate the presence of $Rh^{3+}$ and $Rh^{4+}$, respectively.

Based on the XPS analysis discussed above, the average oxidation state of the B-site Ni and Rh cations weighted by their ratios in $LaNi_{0.99}Rh_{0.01}O_3$ is ~ +2.84 (+2.83 for Ni and +3.28 for Rh), resulting in an oxygen vacancy concentration of 0.16. This is consistent with the reported oxygen vacancy concentration for $LaNiO_3$ generally measured using XPS.[21–23] The difference in the oxygen vacancy concentration estimated from iodometric titrations and XPS could arise from the surface sensitive nature of XPS, which can lead to artifacts in determining the oxygen vacancy concentration due to the undercoordination of

the B-site metal cations in the surface region. However, we note that based on our DFT calculations these oxygen vacancies have limited effect on the ORR energetics. For example, different locations of the oxygen vacancies ($V_O$) in $LaNi_{0.94}Rh_{0.06}O_3$ were investigated (Figure S15). It was found that the surface oxygen vacancies adjacent to Ni cations were energetically most stable. This indicated that the oxygen vacancy defects would form around surface Ni cations away from Rh cations, the proposed active sites for ORR. For OH* adsorption on the most stable oxygen deficient $LaNi_{0.94}Rh_{0.06}O_3$ with surface oxygen vacancies, it was found that OH* adsorption on surface Rh cations was stronger than that on Ni cations with adjacent oxygen vacancies. In addition, the calculated OH* adsorption energy (relative to gas-phase $H_2O$ and $H_2$) on these surface Rh cations was 0.78 eV, with only a 0.03 eV difference as compared to that on the surface Rh cations of the $LaNi_{0.94}Rh_{0.06}O_3$ with no oxygen vacancies. This implies that the oxygen vacancy effect on the ORR activity is not significant, due to the fact that the oxygen vacancies are most stable around Ni cations, rather than near Rh cations, which are the active sites for ORR.

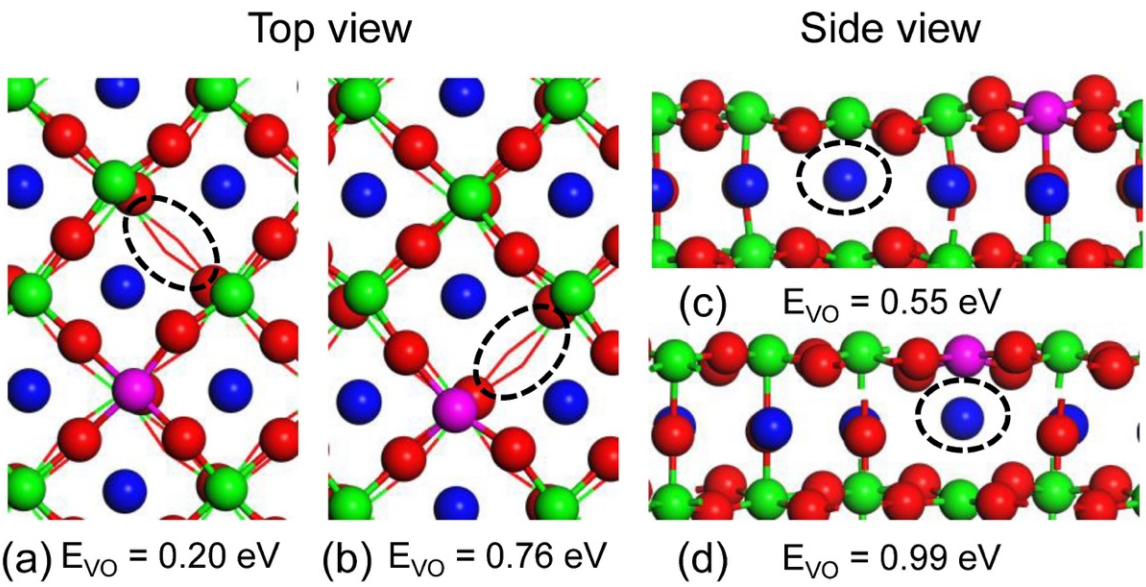


**Figure S15.** Oxygen vacancy ($V_O$) locations depicted using the dashed black cycles in $LaNi_{0.94}Rh_{0.06}O_3$ and the corresponding oxygen vacancy formation energy ($E_{VO}$) with respect to 1/2 $O_2$ in the gas phase: **(a)** a surface oxygen vacancy only coordinated with Ni cations; **(b)** a surface oxygen vacancy coordinated with Ni and Rh cations; **(c)** a subsurface oxygen vacancy only coordinated with Ni cations, and **(d)** a subsurface oxygen vacancy coordinated with surface Rh and subsurface Ni cations. The blue, green, pink, and red spheres represent La, Ni, Rh, and O, respectively.

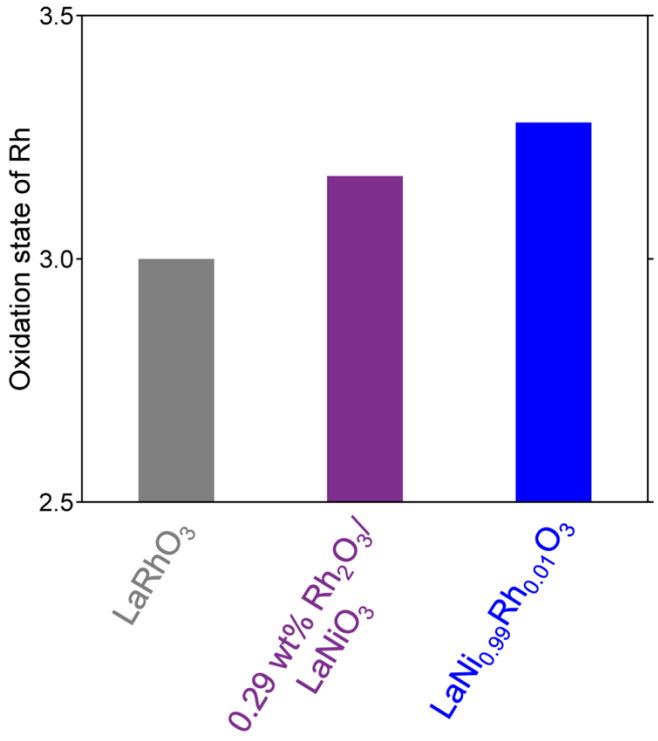


**Figure S16.** The average oxidation state of Rh cations in $LaRhO_3$, 0.29 wt% $Rh_2O_3/LaNiO_3$, and $LaNi_{0.99}Rh_{0.01}O_3$, determined using high resolution XPS of the Rh 3*d* region at a detection depth of ~4.75 nm. It was observed that Rh cations in $LaNi_{0.99}Rh_{0.01}O_3$ were the most oxidized among these oxides.

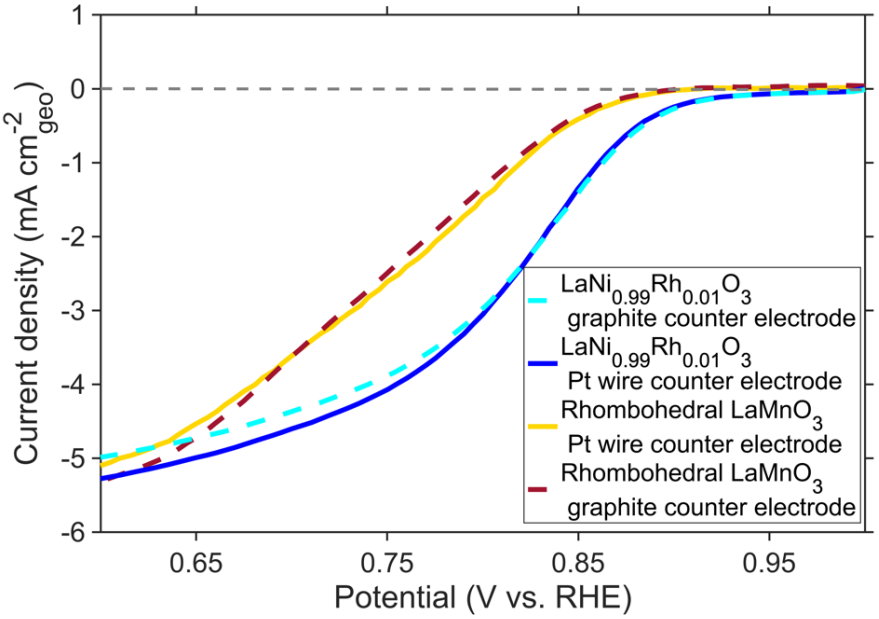


**Figure S17.** Effect of different counter electrodes on the ORR performance of rhombohedral $LaMnO_3$ and $LaNi_{0.99}Rh_{0.01}O_3$. Pt wire and graphite electrode were both investigated as counter electrodes for ORR in background subtracted $O_2$ saturated 0.1M KOH at 1600 revolutions per minute (rpm). No substantial differences in their measured rates were observed for the two systems indicating minimal effect of the counter electrode on the measured electrochemical performance.

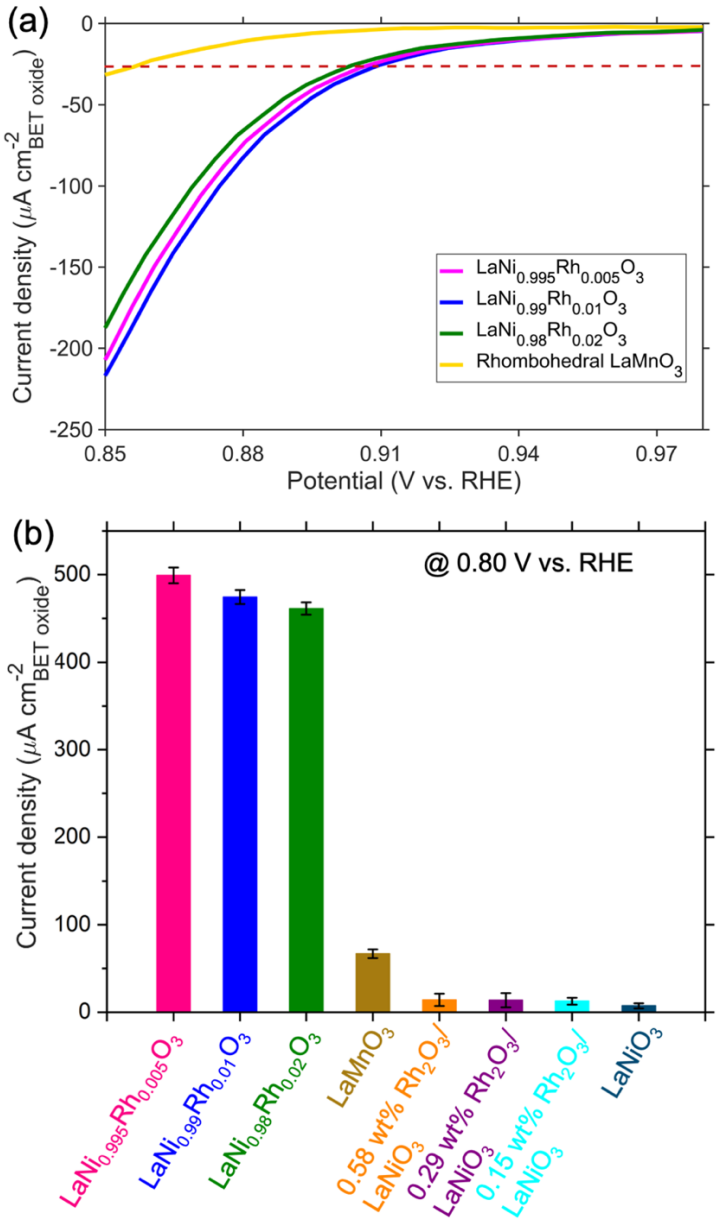


**Figure S18.** Intrinsic activity of various oxides tested in this study. **(a)** Surface area normalized polarization curves for $LaNi_{1-x}Rh_xO_3$ ($0.005 \leq x \leq 0.02$) in comparison with $LaMnO_3$ at 1600 rpm in background subtracted $O_2$-saturated 0.1M KOH. **(b)** The surface area normalized activity at a typical fuel cell operating potential of 0.80 V vs. RHE. It is clearly seen that $LaNi_{0.995}Rh_{0.005}O_3$ exhibits an ~8-fold improvement in the intrinsic activity as compared to $LaMnO_3$ at 0.80 V vs. RHE.

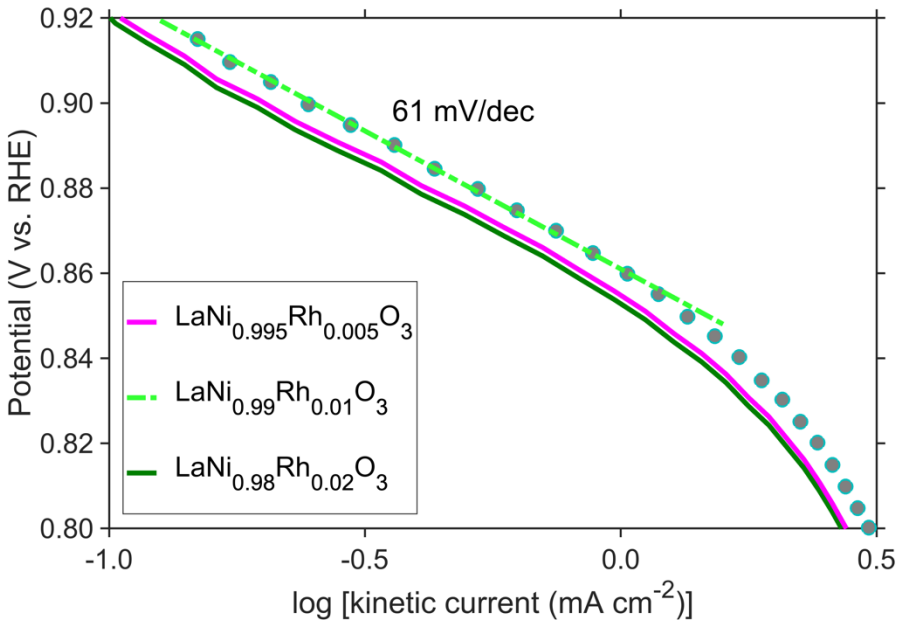


**Figure S19.** Tafel analysis for ORR on $LaNi_{1-x}Rh_xO_3$ ($0.005 \leq x \leq 0.02$), in a potential region between 0.92 and 0.80 V vs. RHE. A Tafel slope of 61 $\pm$ 3 mV/dec was observed for all three perovskite oxides in the kinetic regime, indicating that the first electron transfer was the rate limiting step[24], which was associated with $O_2$ protonation based on our theoretical insights (Fig. S1). These studies showed that $LaNi_{0.99}Rh_{0.01}O_3$ exhibited the highest kinetic current per geometric surface area among these three perovskite oxides. It is important to note that although $LaNi_{0.98}Rh_{0.02}O_3$ had the highest concentration of Rh, it did not lead to the highest kinetic currents. This was potentially due to the formation of less active –Rh–O–Rh– centers as Rh concentration was increased in the structure (more details in the main manuscript).

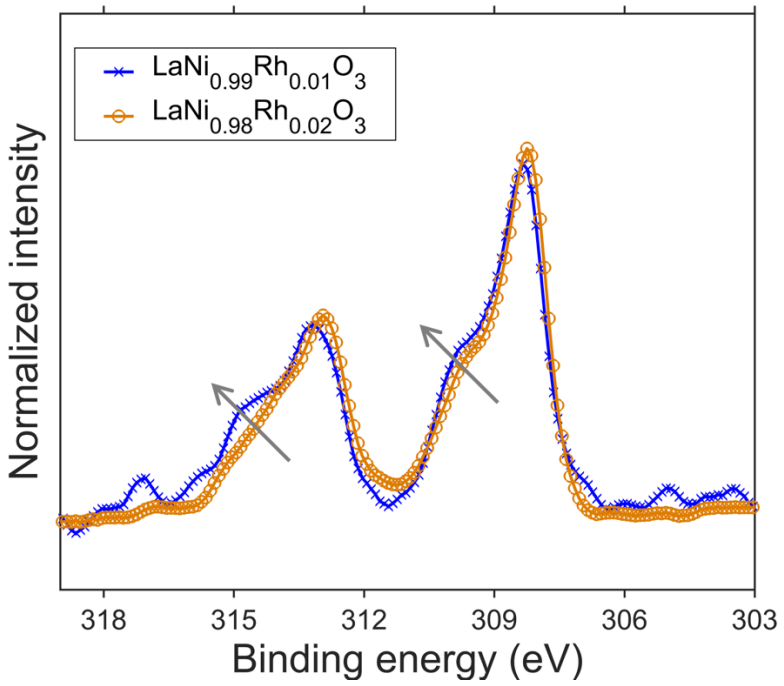


**Figure S20.** HR-XPS spectra of Rh 3*d* core level region for $LaNi_{1-x}Rh_xO_3$ ($x$=0.01 or 0.02) oxides. Cationic Rh in $LaNi_{0.99}Rh_{0.01}O_3$ was found to be more oxidized than in $LaNi_{0.98}Rh_{0.02}O_3$.

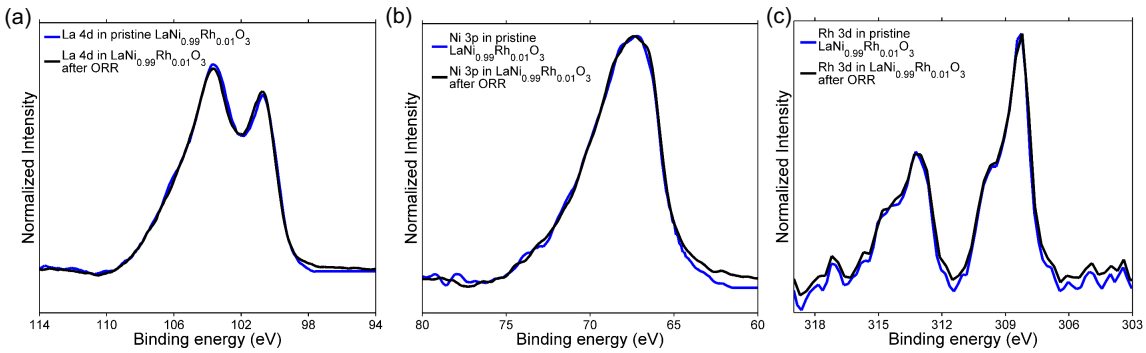


**Figure S21.** Comparison between pristine and post ORR HR-XPS spectra for **(a)** La 4*d*, **(b)** Ni 3*p* and (c) Rh 3*d* indicating negligible changes in the electronic structure of the metal cations. These studies confirm the stability of the metal cations in alkaline environments during electrochemical activity measurements.

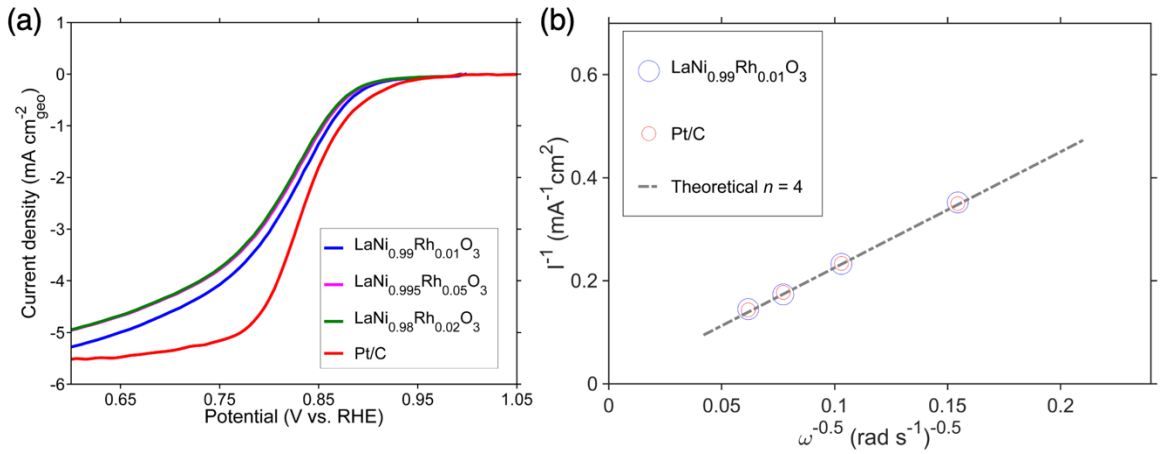


**Figure S22.** ORR activity of $LaNi_{0.995}Rh_{0.005}O_3$, $LaNi_{0.99}Rh_{0.01}O_3$ and $LaNi_{0.98}Rh_{0.02}O_3$ in comparison with the state-of-the-art commercial 20 wt% Pt/C. **(a)** Background subtracted $O_2$-saturated polarization curves in 0.1 M KOH at 1600 rpm. The potentials at 100 $\mu A cm^{-2}_{geo}$ for $LaNi_{0.995}Rh_{0.005}O_3$, $LaNi_{0.99}Rh_{0.01}O_3$ and $LaNi_{0.98}Rh_{0.02}O_3$ were 0.908 $\pm$ 0.003, 0.916 $\pm$ 0.004 and 0.899 $\pm$ 0.004 V vs. RHE, respectively. These values were slightly lower than that of 0.933 $\pm$ 0.004 V vs. RHE for ORR on the commercial 20 wt% Pt/C (details in Table S10). **(b)** Koutecky-Levich (K-L) plot for ORR on $LaNi_{0.99}Rh_{0.01}O_3$ in comparison with commercial 20 wt% Pt/C at 0.60 V vs. RHE. A $4e^-$ transfer ORR process was observed for both systems using K-L analysis.

Koutecky–Levich (K-L) analysis was used to relate the measured current density during ORR to a series of resistances of two major processes: one is associated with the kinetic current which is related to the activity of the catalyst studied, while the other is associated with the mass-diffusion limited regime. The general form of K-L equation is represented by equation 5.

$$\frac{1}{i_m} = \frac{1}{i_k} + \frac{1}{i_{dl}} \qquad \text{(eq. 5)}$$

$i_m$ represents the measured current density for ORR, while, $i_k$ and $i_{dl}$ represent the kinetic and diffusion-limited current densities, respectively.

This analysis can be extended to determine the number of electrons (*n*) transferred during ORR. For instance, Levich equation, as shown in equation 6, relates the diffusion limited current densities to the various parameters as shown below:

$$i_{dl} = 0.62\, n\, F\, C_{O_2} D_{O_2}^{2/3}\, \upsilon^{-1/6}\, \omega^{1/2} = B\, \omega^{1/2} \qquad \text{(eq. 6)}$$

where *n* is the number of electrons transferred during ORR, F is Faraday's constant (96485.3 C/mol), $C_{O_2}$ is the oxygen concentration of a fully saturated 0.1 M KOH electrolyte ($1.21 \times 10^{-6}$ mol/cm$^3$), $D_{O_2}$ is the oxygen diffusivity ($1.9 \times 10^{-5}$ cm$^2$/s), $\upsilon$ is the kinematic viscosity of the electrolyte solution (0.01 cm$^2$/s) and $\omega$ is the rotation rate (rad/s). Consequently, a plot of the measured current density vs. the $\omega^{-0.5}$ can be used to estimate *n*.

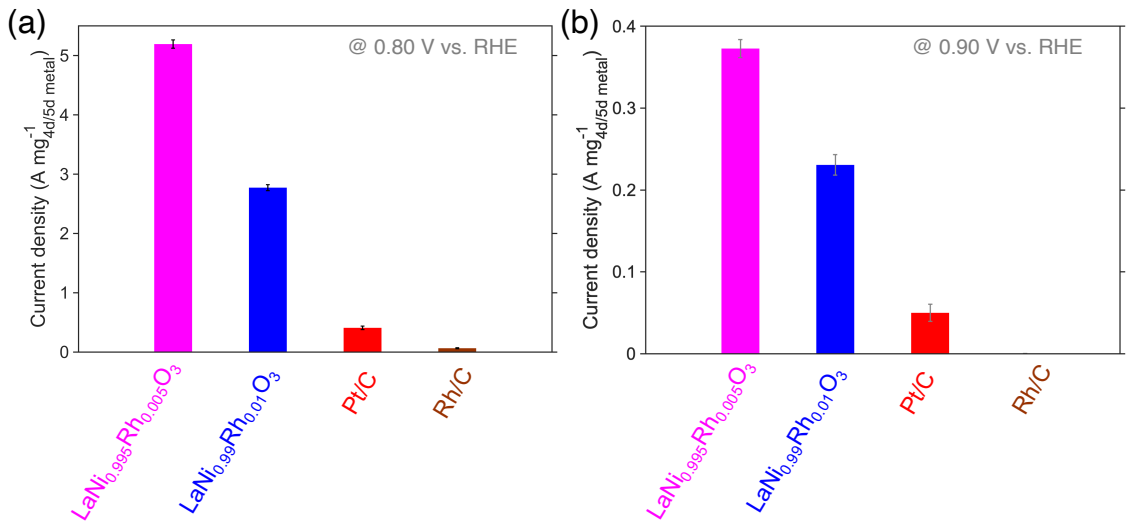


**Figure S23.** Mass activities of $LaNi_{0.995}Rh_{0.005}O_3$, $LaNi_{0.99}Rh_{0.01}O_3$, commercial 20 wt% Pt/C, and commercial 5 wt% Rh/C for ORR at typical fuel cell operating potentials of 0.80 **(a)** and under a kinetic regime at 0.90 V vs. RHE **(b)**.

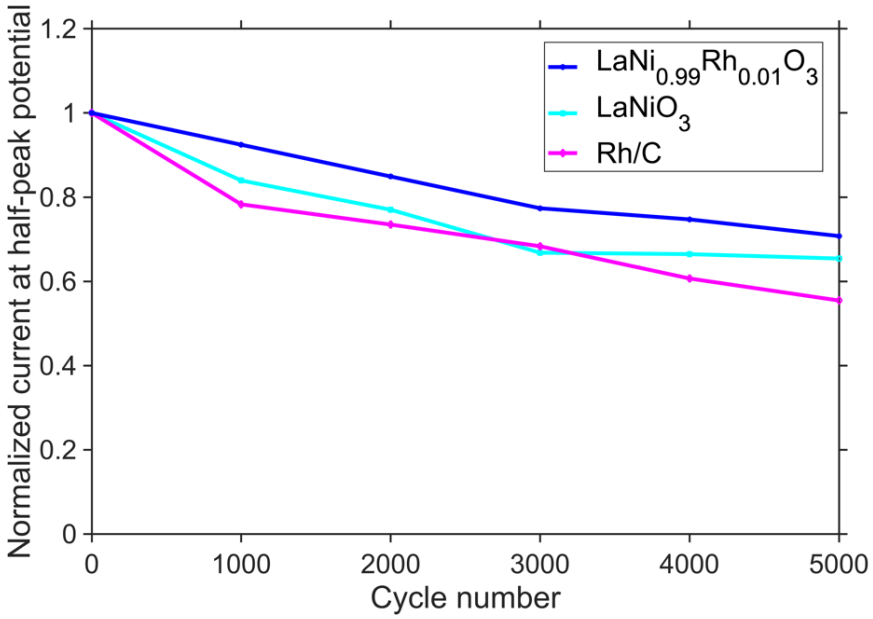


**Figure S24.** Loss in kinetic current at the respective half-peak potential using a standardized United States Department of Energy (DOE) accelerated stability test (AST) for $LaNi_{0.99}Rh_{0.01}O_3$, in comparison with $LaNiO_3$ and commercial 5 wt% Rh/C. The oxides were continuously cycled between 1.0-0.6 V vs. RHE and polarization curves were obtained after every 1000 cycles (~7 hours). The loss in kinetic current for $LaNi_{0.99}Rh_{0.01}O_3$ was the lowest. This enhanced stability of $LaNi_{0.99}Rh_{0.01}O_3$ as compared to $LaNiO_3$ was consistent with the stabilizing role of Rh in these oxides.[25]

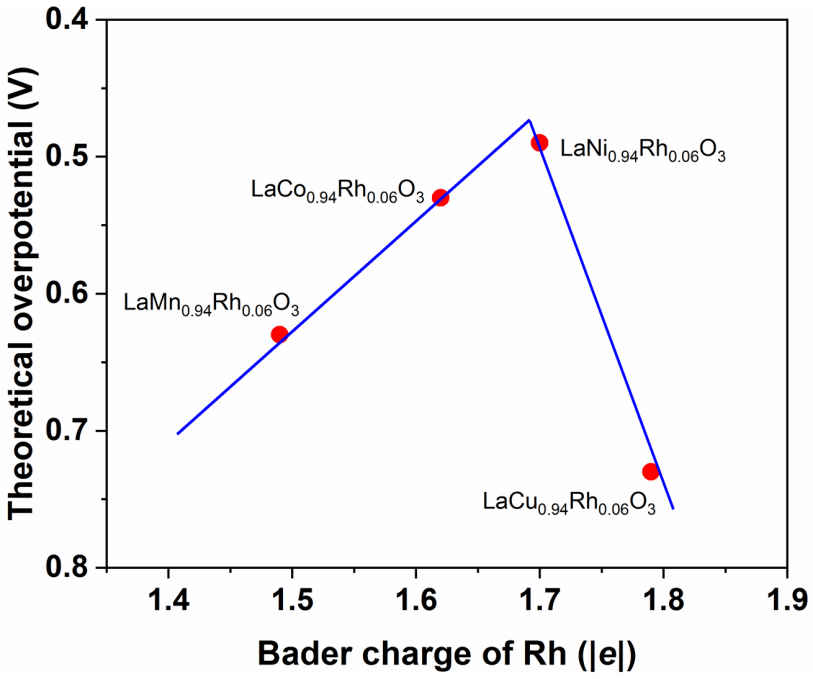


**Figure S25.** Volcano relationship between the calculated theoretical overpotential for ORR on $LaB_{0.94}Rh_{0.06}O_3$ (B = Mn, Co, Ni, Cu) and the Bader charge of surface Rh cations in these oxides. The DFT+U correction for Rh cations was considered using a U correction value of 5.97 eV.

**Table S1.** Calculated adsorption energies of O*, OH*, and OOH* with respect to gas-phase $H_2O$ and $H_2$ on $LaB_{0.94}B'_{0.06}O_3$ (B = Mn, Co, Ni, Cu; B' = Pd, Pt, Rh, Ru, Ir, Os) and $LaRhO_3$. The Bader charges of the surface B' metal cations are also included. Surface B' metal cations are responsible for turning over reactants to products and directly impact the electrocatalytic activity.

| | Adsorption energy (eV) | | | Bader charge |
|---|---|---|---|---|
| | O* | OH* | OOH* | (\|*e*\|) |
| $LaMn_{0.94}Pd_{0.06}O_3$ | 3.51 | 1.07 | 3.98 | +1.08 |
| $LaMn_{0.94}Pt_{0.06}O_3$ | 2.52 | 0.37 | 3.44 | +1.24 |
| $LaMn_{0.94}Rh_{0.06}O_3$ | 1.84 | 0.26 | 3.32 | +1.41 |
| $LaMn_{0.94}Ru_{0.06}O_3$ | 1.25 | -0.18 | 2.89 | +1.94 |
| $LaMn_{0.94}Ir_{0.06}O_3$ | 1.09 | -0.32 | 2.81 | +1.80 |
| $LaMn_{0.94}Os_{0.06}O_3$ | 0.24 | -0.67 | 2.64 | +2.41 |
| $LaCo_{0.94}Pd_{0.06}O_3$ | 3.45 | 1.20 | 4.08 | +1.12 |
| $LaCo_{0.94}Pt_{0.06}O_3$ | 2.68 | 0.69 | 3.75 | +1.33 |
| $LaCo_{0.94}Rh_{0.06}O_3$ | 2.15 | 0.46 | 3.51 | +1.51 |
| $LaCo_{0.94}Ru_{0.06}O_3$ | 1.18 | 0.01 | 3.13 | +1.97 |
| $LaCo_{0.94}Ir_{0.06}O_3$ | 1.26 | -0.14 | 3.05 | +1.81 |
| $LaCo_{0.94}Os_{0.06}O_3$ | 0.29 | -0.35 | 2.84 | +2.66 |
| $LaNi_{0.94}Pd_{0.06}O_3$ | 3.31 | 1.07 | 3.97 | +1.22 |
| $LaNi_{0.94}Pt_{0.06}O_3$ | 2.76 | 0.70 | 3.85 | +1.44 |
| $LaNi_{0.94}Rh_{0.06}O_3$ | 2.45 | 0.75 | 3.79 | +1.64 |

| | | | | |
|---|---|---|---|---|
| $LaNi_{0.94}Ru_{0.06}O_3$ | 1.73 | 0.52 | 3.54 | +2.07 |
| $LaNi_{0.94}Ir_{0.06}O_3$ | 1.91 | 0.37 | 3.46 | +2.01 |
| $LaNi_{0.94}Os_{0.06}O_3$ | 0.97 | 0.05 | 3.29 | +3.05 |
| $LaCu_{0.94}Pt_{0.06}O_3$ | 2.68 | 0.64 | 3.87 | +1.67 |
| $LaCu_{0.94}Rh_{0.06}O_3$ | 2.61 | 0.83 | 3.96 | +1.75 |
| $LaCu_{0.94}Ru_{0.06}O_3$ | 2.03 | 0.75 | 3.86 | +2.19 |
| $LaCu_{0.94}Ir_{0.06}O_3$ | 2.00 | 0.45 | 3.61 | +2.15 |
| $LaRhO_3$ | 1.77 | 0.32 | 3.34 | +1.46 |

**Table S2.** Calculated adsorption energies of O*, OH*, and OOH* with respect to gas-phase $H_2O$ and $H_2$ on $AB_{0.94}B'_{0.06}O_3$ (A = Y, Pr; B = Co, Ni; B' = Pd, Pt, Rh, Ru, Ir, Os) oxides.

| | Adsorption energy (eV) | | |
|---|---|---|---|
| | O* | OH* | OOH* |
| $YNi_{0.94}Pd_{0.06}O_3$ | 3.38 | 1.06 | 4.11 |
| $YNi_{0.94}Pt_{0.06}O_3$ | 2.53 | 0.53 | 3.63 |
| $YNi_{0.94}Rh_{0.06}O_3$ | 2.41 | 0.66 | 3.68 |
| $YNi_{0.94}Ru_{0.06}O_3$ | 1.54 | 0.47 | 3.50 |
| $YNi_{0.94}Ir_{0.06}O_3$ | 1.70 | 0.30 | 3.37 |
| $YNi_{0.94}Os_{0.06}O_3$ | 0.65 | -0.09 | 3.03 |
| $PrNi_{0.94}Pd_{0.06}O_3$ | 3.36 | 1.11 | 3.99 |
| $PrNi_{0.94}Pt_{0.06}O_3$ | 2.63 | 0.68 | 3.77 |
| $PrNi_{0.94}Rh_{0.06}O_3$ | 2.38 | 0.72 | 3.77 |
| $PrNi_{0.94}Ru_{0.06}O_3$ | 1.63 | 0.49 | 3.57 |
| $PrNi_{0.94}Ir_{0.06}O_3$ | 1.80 | 0.40 | 3.50 |
| $PrNi_{0.94}Os_{0.06}O_3$ | 0.82 | 0.13 | 3.20 |
| $YCo_{0.94}Pd_{0.06}O_3$ | 3.67 | 1.32 | 4.18 |
| $YCo_{0.94}Pt_{0.06}O_3$ | 2.90 | 0.79 | 4.04 |
| $YCo_{0.94}Rh_{0.06}O_3$ | 2.53 | 0.76 | 3.94 |
| $YCo_{0.94}Ru_{0.06}O_3$ | 1.60 | 0.27 | 3.37 |
| $YCo_{0.94}Ir_{0.06}O_3$ | 1.64 | 0.21 | 3.42 |

| | | | |
|---|---|---|---|
| $YCo_{0.94}Os_{0.06}O_3$ | 0.32 | -0.33 | 2.89 |
| $PrCo_{0.94}Pd_{0.06}O_3$ | 3.45 | 1.21 | 4.08 |
| $PrCo_{0.94}Pt_{0.06}O_3$ | 2.79 | 0.68 | 3.73 |
| $PrCo_{0.94}Rh_{0.06}O_3$ | 2.12 | 0.45 | 3.58 |
| $PrCo_{0.94}Ru_{0.06}O_3$ | 1.14 | -0.02 | 3.14 |
| $PrCo_{0.94}Ir_{0.06}O_3$ | 1.25 | -0.10 | 3.06 |
| $PrCo_{0.94}Os_{0.06}O_3$ | 0.28 | -0.38 | 2.85 |

**Table S3.** Calculated tolerance factors for $LaB_{1-x}B'_xO_3$ (B = Mn, Co, Ni; B' = Ru, Rh, Pd, Ir; $x$ = 0, 0.01 or 1) oxides.

| Composition | Tolerance Factor | |
|---|---|---|
| | **Goldschmidt (*t*)** | **Bartel et al., (τ)** |
| $LaMnO_3$ | 0.985 | 1.668 |
| $LaCoO_3$ | 1.003 | 1.755 |
| $LaNiO_3$ | 0.996 | 1.711 |
| $LaRuO_3$ | 0.938 | 1.715 |
| $LaRhO_3$ | 0.945 | 1.681 |
| $LaPdO_3$ | 0.904 | 2.067 |
| $LaIrO_3$ | 0.938 | 1.715 |
| $LaMn_{0.99}Ru_{0.01}O_3$ | 0.954 | 1.650 |
| $LaMn_{0.99}Rh_{0.01}O_3$ | 0.954 | 1.650 |
| $LaMn_{0.99}Pd_{0.01}O_3$ | 0.954 | 1.651 |
| $LaMn_{0.99}Ir_{0.01}O_3$ | 0.954 | 1.650 |
| $LaCo_{0.99}Ru_{0.01}O_3$ | 1.003 | 1.751 |
| $LaCo_{0.99}Rh_{0.01}O_3$ | 1.003 | 1.752 |
| $LaCo_{0.99}Pd_{0.01}O_3$ | 1.002 | 1.745 |
| $LaCo_{0.99}Ir_{0.01}O_3$ | 1.003 | 1.751 |
| $LaNi_{0.99}Ru_{0.01}O_3$ | 0.995 | 1.708 |
| $LaNi_{0.99}Rh_{0.01}O_3$ | 0.995 | 1.708 |

| | | |
|---|---|---|
| $LaNi_{0.99}Pd_{0.01}O_3$ | 0.994 | 1.703 |
| $LaNi_{0.99}Ir_{0.01}O_3$ | 0.995 | 1.708 |

To evaluate the phase stability of $LaB_{1-x}B'_xO_3$ (B = Mn, Co, Ni; B' = Ru, Rh, Pd, Ir; $x$=0, 0.01 or 1) perovskites, their tolerance factors (Goldschmidt tolerance factor[26] and the newly developed tolerance factor by Bartel and co-worker[25]) were calculated. It is worth noting that Pt and Os generally exhibit +2/+4 and > +4 oxidation states, respectively. This results in challenges with incorporation of Pt and Os in the B-site of $LaBO_3$ (B = Mn, Co, Ni) perovskites due to charge imbalance, resulting in phase separation. Although creating cationic defects in these perovskites have been used to incorporate Pt in the B site, they were often challenged with phase instability under reaction conditions especially when La is used as the A-site.[27] Hence, Pt and Os were not considered in this analysis. Conversely, Ru, Rh, Pd and Ir exhibit favorable +3 oxidation states, which facilitates charge balance when they are incorporated in the B-site of $LaBO_3$ (B = Mn, Co, Ni) perovskites. Therefore, $LaB_{1-x}B'_xO_3$ (B = Mn, Co, Ni; B' = Ru, Rh, Pd, Ir) oxides were considered in this analysis.

The values for the Goldschmidt ($t$) and Bartel ($\tau$) tolerance factors were obtained using the equations $t = \frac{(r_A+r_O)}{\sqrt{2}\,(r_B+r_O)}$ and $\tau = \frac{r_O}{r_B} - n_A\left[n_A - \frac{\frac{r_A}{r_B}}{\ln\left(\frac{r_A}{r_B}\right)}\right]$, respectively. $r_A$, $r_B$ and $r_O$ represent the ionic radii of the A-site metal (twelve-fold coordination), B-site metal (six-fold coordination) and lattice oxygen, respectively. $n_A$ represents the oxidation state of the A-site metal. The corresponding ionic radii were obtained from revised Shannon's database of ionic radii.[28] It is important to note that both Co and Ni are present in a low

spin state in $LaCoO_3$ and $LaNiO_3$, respectively, while Mn is present in a high spin state in $LaMnO_3$.[29–31] Thus, the corresponding ionic radii of $Co^{3+}$ and $Ni^{3+}$ in low spin and $Mn^{3+}$ in high spin were used in calculating the tolerance factors. For the mixed B-site compositions (e.g., $LaB_{0.99}B'_{0.01}O_3$), $r_B$ was approximated to be the weighted average (based on at %) of the radii of the B and B' cations. A high phase stability is characterized by a value of Goldschmidt tolerance factor ($t$) ranging from 0.825 to 1.059.[25,26] However, one of the primary challenges with using $t$ is its limited accuracy of 83%. On the other hand, the newly developed tolerance factor, $\tau$, by Bartel et al., takes advantage of machine learning based algorithms to predict the probability of phase stability of the perovskite, with a high accuracy of 92%. Generally, a $\tau$ value smaller than 4.18 indicates a stable phase for perovskite oxide. As the $\tau$ value decreases, the probability of phase stability of the perovskite increases. The probability of stability ($P(\tau)$) was extrapolated from ref. [25] based on the values of $\tau$. In short, $P(\tau)$ was estimated based on Plack's scaling using binary classification of perovskite/non-perovskite structures which was transformed into a continuous probability estimation of the perovskite stability. For instance, perovskites with $\tau$ values lower than 2, exhibited $P(\tau)>0.95$.

**Table S4.** BET physical surface areas of the oxides measured via $N_2$ physisorption at 77K.

| Oxide target composition | Surface area ($m^2/g$) |
|---|---|
| $LaNi_{0.995}Rh_{0.005}O_3$ | $2.19 \pm 0.28$ |
| $LaNi_{0.99}Rh_{0.01}O_3$ | $2.45 \pm 0.34$ |
| $LaNi_{0.98}Rh_{0.02}O_3$ | $2.29 \pm 0.18$ |
| 0.15 wt% $Rh_2O_3/LaNiO_3$ | $2.32 \pm 0.39$ |
| 0.29 wt% $Rh_2O_3/LaNiO_3$ | $2.41 \pm 0.41$ |
| 0.58 wt% $Rh_2O_3/LaNiO_3$ | $2.26 \pm 0.22$ |
| $LaNiO_3$ | $2.96 \pm 0.39$ |

**Table S5.** Experimentally measured concentrations of all elements via energy dispersive X-ray spectroscopy (EDS) using transmission electron microscopy.

| Sample | Element | Atomic concentration (%) |
|---|---|---|
| $LaNi_{0.99}Rh_{0.01}O_3$ | Rh (L-edge) | 1.08 |
| | La (L-edge) | 49.95 |
| | Ni (K-edge) | 48.97 |
| 0.29 wt% $Rh_2O_3/LaNiO_3$ | Rh (L-edge) | 1.10% |
| | La (L-edge) | 49.96% |
| | Ni (K-edge) | 48.94% |
| $LaNi_{0.99}Rh_{0.02}O_3$ | Rh (L-edge) | 1.94% |
| | La (L-edge) | 50.04% |
| | Ni (K-edge) | 48.02% |

**Table S6.** Rh content in different oxides determined using inductively coupled plasma mass spectrometry (ICP-MS).

| **Oxide target composition** | **Measured Rh concentration (wt%)** |
|---|---|
| $LaNi_{0.995}Rh_{0.005}O_3$ | $0.15 \pm 0.008$ |
| 0.5 at% $Rh_2O_3/LaNiO_3$ | $0.15 \pm 0.006$ |
| $LaNi_{0.99}Rh_{0.01}O_3$ | $0.29 \pm 0.01$ |
| 1 at% $Rh_2O_3/LaNiO_3$ | $0.29 \pm 0.01$ |
| $LaNi_{0.98}Rh_{0.02}O_3$ | $0.59 \pm 0.02$ |
| 2 at% $Rh_2O_3/LaNiO_3$ | $0.58 \pm 0.03$ |

**Table S7.** Quantification of the Ni and Rh concentrations in the various oxides based on AR-XPS, over detection depths (*d*) of 1.6 to 4.75 nm.

| Sample | Detection depth / angle | Concentration of Ni (at %) | Concentration of Rh (at %) |
|---|---|---|---|
| $LaNi_{0.99}Rh_{0.01}O_3$ | 4.75 nm / 0° | 98.9% | 1.1% |
| | 4.1 nm / 35° | 99.1% | 0.9% |
| | 1.6 nm / 70 ° | 99.0 | 1.0 |
| 0.29 wt% $Rh_2O_3/LaNiO_3$ | 4.75 nm / 0° | 92.0% | 8.0% |
| | 4.1 nm / 35° | 91.9% | 8.1% |
| | 1.6 nm / 70 ° | 91.0% | 9.1% |
| $LaNi_{0.98}Rh_{0.02}O_3$ | 4.75 nm / 0° | 97.9% | 2.1% |
| | 4.1 nm / 35° | 98.9% | 1.9% |
| | 1.6 nm / 70 ° | 98.3% | 1.7% |
| 0.58 wt% $Rh_2O_3/LaNiO_3$ | 4.75 nm / 0° | 84.8% | 15.2% |
| | 4.1 nm / 35° | 86% | 14.0% |
| | 1.6 nm / 70 ° | 86.2% | 13.8% |

**Table S8.** Measured potentials for ORR on various oxides at 100 $\mu Acm^{-2}_{geo}$ in $O_2$ saturated 0.1M KOH. The background currents were corrected via Ar-saturated studies, and subsequent subtracted from $O_2$-saturated measurements.

| **Composition** | **Potential to achieve 100 $\mu Acm^{-2}_{geo}$ (V *vs.* RHE)** |
|---|---|
| $LaNi_{0.995}Rh_{0.005}O_3$ | 0.908 ± 0.003 |
| $LaNi_{0.99}Rh_{0.01}O_3$ | 0.916 ± 0.004 |
| $LaNi_{0.98}Rh_{0.02}O_3$ | 0.899 ± 0.004 |
| $LaNiO_3$ | 0.774 ± 0.006 |
| $LaRhO_3$ | 0.752 ± 0.008 |
| 0.15 wt % $Rh_2O_3/LaNiO_3$ | 0.793 ± 0.009 |
| 0.29 wt % $Rh_2O_3/LaNiO_3$ | 0.789 ± 0.005 |
| 0.58 at % $Rh_2O_3/LaNiO_3$ | 0.790 ± 0.005 |
| $LaMnO_3$ | 0.887 ± 0.003 |
| 5 wt% Rh/C | 0.801 ± 0.005 |
| 20 wt% Pt/C | 0.933 ± 0.004 |

**Table S9.** Reported activity of $LaNiO_3$ for ORR in $O_2$-saturated 0.1 M KOH at 1600 rpm normalized per geometric area of the electrode, in comparison with the oxide surface area, as well as the oxide loading on the electrode.

| **Literature report** | **$LaNiO_3$ loading on the composite electrode ($\mu g\ cm^{-2}_{geo}$)** | **Surface area of $LaNiO_3$ ($m^2g^{-1}$)** | **Potential required to achieve 100 $\mu Acm^{-2}_{geo}$ (V vs. RHE)** |
|---|---|---|---|
| Celorrio, V., et al., ChemElectroChem, 2016, 3, 283-291 | 250 | 29.1 | 0.738 |
| Goodenough, J. B., et al., J. Mater. Chem. A, 2015, 3, 9421-9426 | 200 | NA | 0.695 |
| Stevenson, K., et al., Chem. Mater., 2014, 26, 3368-3376 | 15.3 | 11 | 0.741 |
| Sunarso, S., et al., Chem., - Eur. J., 2016, 22, 2719-2727 | 232 | 2.97 | 0.74 |
| Shui, J., et al., Scientific Reports, 2016, 6, 24314 | 38.28 | NA | 0.789 |
| Huang, et al., RSC Adv., 2016, 6, 86386-86394 | 84.6 | 30.612 | 0.770 |
| Hardin, W., et al., J. Phys. Chem. Lett., 2013, 4, 1254-1259 | 51.02 | 6 | 0.725 |
| Sunarso, J., et al., J. Phys. Chem. Lett., 2013, 4, 2982-2988 | 264.55 | 3.8 | 0.774 |
| This work | 250 | 2.45 | 0.773 |

**Table S10.** Detection limits for ICP-MS analysis of La, Ni, Rh and Pt as determined using the standard solutions employed for calibrations.

| Element | Detection limit (ppb or ng/mL) |
|---|---|
| La | 0.040 |
| Ni | 1.000 |
| Rh | 0.155 |
| Pt | 0.030 |

The detection limit of the ICP-MS studies was also expressed in terms of oxide atomic layer equivalent using the example of $LaNi_{0.99}Rh_{0.01}O_3$ as shown below:

- Oxide loading per film = 250 $\mu g cm^{-2}_{geo}$ (geo refers to the geometric area of the electrode).
- Diameter of the electrode = 5 mm
- Area of the electrode = 0.1963 $cm^2$
- Volume of electrolyte = 40 mL
- The total amount of Rh in each film of $LaNi_{0.99}Rh_{0.01}O_3$ = $0.0029*250 \frac{\mu g}{cm^2} *0.196\ cm^2 = 142.1$ ng. In the scenario that all the Rh cations in the film are dissolved into the electrolyte, then $= \frac{142.1\ ng}{40\ mL} = 3.5525$ ng/mL. The detection limit for ICP-MS of Rh is 0.155 $\frac{ng}{mL}$ ==> $0.155 \frac{ng}{mL} *40$ mL = 6.2 ng. This

implies that the total amount of Rh in the film is ~23 times higher than the detection limit.

- Density of $LaNi_{0.99}Rh_{0.01}O_3$, $\rho_{oxide}$= 6.93 g $cm^{-3}$
- Lattice parameters as measured using X-ray diffraction for $LaNi_{0.99}Rh_{0.01}O_3$, a = b = 5.45 Å
- BET Surface area of $LaNi_{0.99}Rh_{0.01}O_3$ = 2.45 $\pm$ 0.34 $m^2g^{-1}$
- ∴ Available oxide surface area = $250 \frac{\mu g_{oxide}}{cm^2_{geo}}$ *0.196 $cm^2_{geo}$* $\frac{2.45*10^4 cm^2_{oxide}}{10^6\ \mu g_{oxide}}$ =1.2005 $cm^2_{oxide}$
- ∴ Mass of oxide dissolution per monolayer (ML) = $\rho_{oxide}$* available surface area = 6.93 $\frac{g}{cm^3}$ *1.2005 $cm^2$=8.32 $\frac{g}{cm}$ =83.2 $\frac{ng}{Å}$
- Based on lattice parameter, a = 5.45 Å; mass of oxide dissolution per ML = 83.2 $\frac{ng}{Å}$ * 5.45 Å = 453.44 ng per ML
- Since the weight loading of Rh in $LaNi_{0.99}Rh_{0.01}O_3$ is 0.29 wt% == > 1.32 $ng_{Rh}$; this implies that the detection limit of ICP-MS is equivalent to 4.7 MLs of Rh content in $LaNi_{0.99}Rh_{0.01}O_3$.

Similar analysis was extended to $LaNi_{0.98}Rh_{0.02}O_3$, and the ICP-MS detection limit was found to be ~2.5 MLs of oxide Rh content. On the other hand, in the case of $LaRhO_3$, dissolution of even one ML of Rh from the top surface layer would be detectable due to the high concentration of Rh in this oxide.

## SI References


(1) Kresse, G.; Furthmüller, J. Efficient Iterative Schemes for Ab Initio Total-Energy Calculations Using a Plane-Wave Basis Set. *Phys. Rev. B Condens. Matter Mater. Phys.* **1996**, *54*, 11169–11186. https://doi.org/10.1103/PhysRevB.54.11169.

(2) Kresse, G.; Furthmüller, J. Efficiency of Ab-Initio Total Energy Calculations for Metals and Semiconductors Using a Plane-Wave Basis Set. *Comput. Mater. Sci.* **1996**, *6*, 15–50. https://doi.org/10.1016/0927-0256(96)00008-0.

(3) Perdew, J. P.; Burke, K.; Ernzerhof, M. Generalized Gradient Approximation Made Simple. *Phys. Rev. Lett.* **1996**, *77*, 3865–3868. https://doi.org/10.1103/PhysRevLett.77.3865.

(4) Samira, S.; Gu, X. K.; Nikolla, E. Design Strategies for Efficient Nonstoichiometric Mixed Metal Oxide Electrocatalysts: Correlating Measurable Oxide Properties to Electrocatalytic Performance. *ACS Catal.* **2019**, *9*, 10575–10586. https://doi.org/10.1021/acscatal.9b02505.

(5) Yoo, J. S.; Rong, X.; Liu, Y.; Kolpak, A. M. Role of Lattice Oxygen Participation in Understanding Trends in the Oxygen Evolution Reaction on Perovskites. *ACS Catal.* **2018**, *8*, 4628–4636. https://doi.org/10.1021/acscatal.8b00612.

(6) Xu, Z.; Rossmeisl, J.; Kitchin, J. R. A Linear Response DFT+U Study of Trends in the Oxygen Evolution Activity of Transition Metal Rutile Dioxides. *J. Phys. Chem. C* **2015**, *119*, 4827–4833. https://doi.org/10.1021/jp511426q.

(7) Zeng, Z.; Chan, M. K. Y.; Zhao, Z. J.; Kubal, J.; Fan, D.; Greeley, J. Towards First Principles-Based Prediction of Highly Accurate Electrochemical Pourbaix Diagrams. *J. Phys. Chem. C* **2015**, *119*, 18177–18187. https://doi.org/10.1021/acs.jpcc.5b03169.

(8) Nørskov, J. K.; Rossmeisl, J.; Logadottir, A.; Lindqvist, L.; Kitchin, J. R.; Bligaard, T.; Jónsson, H. Origin of the Overpotential for Oxygen Reduction at a Fuel-Cell Cathode. *J. Phys. Chem. B* **2004**, *108*, 17886–17892. https://doi.org/10.1021/jp047349j.

(9) Rivas, M. E.; Fierro, J. L. G.; Goldwasser, M. R.; Pietri, E.; Pérez-Zurita, M. J.; Griboval-Constant, A.; Leclercq, G. Structural Features and Performance of $LaNi_{1-x}Rh_xO_3$ System for the Dry Reforming of Methane. *Appl. Catal. A* **2008**, *344*, 10–19. https://doi.org/10.1016/j.apcata.2008.03.023.

(10) Johansson, T.; Pakhare, D.; Haynes, D.; Abdelsayed, V.; Shekhawat, D.; Spivey, J. Characterization of $LaRhO_3$ Perovskites for Dry ($CO_2$) Reforming of Methane (DRM). *Chem. Pap.* **2014**, *68*, 1240–1247. https://doi.org/10.2478/s11696-014-0566-2.

(11) Carneiro, J. S. A.; Williams, J.; Gryko, A.; Herrera, L. P.; Nikolla, E. Embracing the Complexity of Catalytic Structures: A Viewpoint on the Synthesis of Nonstoichiometric Mixed Metal Oxides for Catalysis. *ACS Catal.* **2020**, *10*, 516–527. https://doi.org/10.1021/acscatal.9b04226.

(12) Brauer, G. *Handbook of Preparative Inorganic Chemistry*; 1964. https://doi.org/10.1016/b978-0-12-395590-6.x5001-7.

(13) Druce, J.; Téllez, H.; Burriel, M.; Sharp, M. D.; Fawcett, L. J.; Cook, S. N.; McPhail, D. S.; Ishihara, T.; Brongersma, H. H.; Kilner, J. A. Surface Termination and Subsurface Restructuring of Perovskite-Based Solid Oxide Electrode Materials.

*Energy Environ. Sci.* **2014**, *7*, 3593–3599. https://doi.org/10.1039/c4ee01497a.
(14) Merzlikin, S. Depth Profiling by X-Ray Photoelectron Spectroscopy, Ruhr-Universität Bochum, 2007.
(15) Gulino, A.; Egdell, R. G.; Fragalà, I. Mechanically Induced Phase Transformation and Surface Segregation in Bismuth-Doped Tetragonal Zirconia. *J. Am. Ceram. Soc.* **1998**, *81*, 757–759. https://doi.org/10.1111/j.1151-2916.1998.tb02406.x.
(16) Cristaldi, D. A.; Impellizzeri, G.; Priolo, F.; Gupta, T.; Gulino, A. Structural, Electronic, and Electrical Properties of Y-Doped $Cd_2SnO_4$. *J. Phys. Chem. C* **2012**, *116*, 3363–3368. https://doi.org/10.1021/jp2103676.
(17) Silversmit, G.; Depla, D.; Poelman, H.; Marin, G. B.; De Gryse, R. Determination of the V2*p* XPS Binding Energies for Different Vanadium Oxidation States ($V^{5+}$ to $V^{0+}$). *J. Electron Spectros. Relat. Phenomena* **2004**, *135*, 167–175. https://doi.org/10.1016/j.elspec.2004.03.004.
(18) Samira, S.; Camayang, J. C. A.; Nacy, A. M.; Diaz, M.; Meira, S. M.; Nikolla, E. Electrochemical Oxygen Reduction on Layered Mixed Metal Oxides: Effect of B-Site Substitution. *J. Electroanal. Chem.* **2019**, *833*, 490–497. https://doi.org/10.1016/j.jelechem.2018.12.023.
(19) Su, H. Y.; Gorlin, Y.; Man, I. C.; Calle-Vallejo, F.; Norskov, J. K.; Jaramillo, T. F.; Rossmeisl, J. Identifying Active Surface Phases for Metal Oxide Electrocatalysts: A Study of Manganese Oxide Bi-Functional Catalysts for Oxygen Reduction and Water Oxidation Catalysis. *Phys. Chem. Chem. Phys.* **2012**, *14*, 14010–10422. https://doi.org/10.1039/c2cp40841d.
(20) Kundu, M. K.; Mishra, R.; Bhowmik, T.; Barman, S. Rhodium Metal-Rhodium Oxide (Rh-$Rh_2O_3$) Nanostructures with Pt-like or Better Activity towards Hydrogen Evolution and Oxidation Reactions (HER, HOR) in Acid and Base: Correlating Its HOR/HER Activity with Hydrogen Binding Energy and Oxophilicity of the Cat. *J. Mater. Chem. A* **2018**, *6*, 23531–23541. https://doi.org/10.1039/c8ta07028h.
(21) Qiao, L.; Bi, X. Direct Observation of $Ni^{3+}$ and $Ni^{2+}$ in Correlated $LaNiO_{3-\delta}$ Films. *Euro. Phys. Lett.* **2011**, *93*, 57002. https://doi.org/10.1209/0295-5075/93/57002.
(22) Xu, J.; Sun, C.; Wang, Z.; Hou, Y.; Ding, Z.; Wang, S. Perovskite Oxide $LaNiO_3$ Nanoparticles for Boosting $H_2$ Evolution over Commercial CdS with Visible Light. *Chem. - Eur. J.* **2018**, *24*, 18512–18517. https://doi.org/10.1002/chem.201802920.
(23) Pereñíguez, R.; González-DelaCruz, V. M.; Holgado, J. P.; Caballero, A. Synthesis and Characterization of a $LaNiO_3$ Perovskite as Precursor for Methane Reforming Reactions Catalysts. *Appl. Catal. B* **2010**, *93*, 346–353. https://doi.org/10.1016/j.apcatb.2009.09.040.
(24) Holewinski, A.; Linic, S. Elementary Mechanisms in Electrocatalysis: Revisiting the ORR Tafel Slope. *J. Electrochem. Soc.* **2012**, *159*, H864–H870. https://doi.org/10.1149/2.022211jes.
(25) Bartel, C. J.; Sutton, C.; Goldsmith, B. R.; Ouyang, R.; Musgrave, C. B.; Ghiringhelli, L. M.; Scheffler, M. New Tolerance Factor to Predict the Stability of Perovskite Oxides and Halides. *Sci. Adv.* **2019**, *5*, eaav0693. https://doi.org/10.1126/sciadv.aav0693.
(26) Goldschmidt, V. M. Die Gesetze Der Krystallochemie. *Naturwissenschaften* **1926**, *14*, 477–485. https://doi.org/10.1007/BF01507527.
(27) Katz, M. B.; Zhang, S.; Duan, Y.; Wang, H.; Fang, M.; Zhang, K.; Li, B.; Graham,

G. W.; Pan, X. Reversible Precipitation/Dissolution of Precious-Metal Clusters in Perovskite-Based Catalyst Materials: Bulk versus Surface Re-Dispersion. *J. Catal.* **2012**, *293*, 145–148. https://doi.org/10.1016/j.jcat.2012.06.017.

(28) Shannon, R. D. Revised Effective Ionic Radii and Systematic Studies of Interatomic Distances in Halides and Chalcogenides. *Acta Crystallogr. Sect. A* **1976**, *32*, 751–767. https://doi.org/10.1107/S0567739476001551.

(29) Yan, J. Q.; Zhou, J. S.; Goodenough, J. B. Bond-Length Fluctuations and the Spin-State Transition in $LCoO_3$ (L=La, Pr, and Nd). *Phys. Rev. B Condens. Matter Mater. Phys.* **2004**, *69*, 134409. https://doi.org/10.1103/PhysRevB.69.134409.

(30) Zhou, J.; Goodenough, J.; Dabrowski, B.; Klamut, P.; Bukowski, Z. Probing the Metal-Insulator Transition in Ni(III)-Oxide Perovskites. *Phys. Rev. B Condens. Matter Mater. Phys.* **2000**, *61*, 4401–4404. https://doi.org/10.1103/PhysRevB.61.4401.

(31) Töpfer, J.; Goodenough, J. B. $LaMnO_{3+\delta}$ Revisited. *J. Solid State Chem.* **1997**, *130*, 117–128. https://doi.org/10.1006/jssc.1997.7287.